The ion microprobe as a tool for obtaining strontium isotopes in magmatic plagioclase: A case study at Okataina Volcanic Centre, New Zealand

May Sas[1*], Noriyuki Kawasaki[2], Naoya Sakamoto[3], Phil Shane[1], Georg F. Zellmer[4], Adam J. R. Kent[5], Hisayoshi Yurimoto[2,3]

[1]School of Environment, University of Auckland, Private Bag 92019, Auckland 1142, New Zealand

[2]Natural History Sciences, Hokkaido University, Sapporo 060-0810, Japan

[3]Isotope Imaging Laboratory, Creative Research Institution, Hokkaido University, Sapporo 001-0021, Japan

[4]Volcanic Risk Solutions, Massey University, Private Bag 11222, Palmerston North 4442, New Zealand

[5]College of Earth, Ocean, and Atmospheric Sciences, Oregon State University, Corvallis, Oregon 97330, USA

*Corresponding author. E-mail address: msas481@aucklanduni.ac.nz (M. Sas)

Declaration of interest: none

Abstract

We investigated the potential of multi-collector secondary ion mass spectrometry (MC-SIMS) as a tool for obtaining Sr isotopic compositions in plagioclase, a ubiquitous mineral in igneous rocks that serves as a recorder of crystallisation history. MC-SIMS allows for high spatial resolution analysis (~12 μm in this study) of isotopes, and therefore improves the temporal scale at which fluctuations in crystallization conditions can be recognized, ultimately improving our understanding of rates of magmatic processes. Plagioclase crystals from two young rhyolitic deposits from two major eruptive complexes, Tarawera and Haroharo, of the Okataina Volcanic Centre in New Zealand were analysed. Results were corrected for matrix effects using linear modelling of MC-SIMS data versus An contents, as well as $^{87}Sr/^{86}Sr$ ratios acquired via laser ablation inductively-coupled plasma mass spectrometry (LA-MC-ICP-MS). Corrected MC-SIMS Sr isotopic ratios had an average 2σ uncertainty of ± 0.0008 per spot, and were homogeneous in Okataina plagioclase at high spatial resolutions. Average LA-MC-ICP-MS $^{87}Sr/^{86}Sr$ ratios of plagioclase from both intra-caldera volcanic complexes (Tarawera $^{87}Sr/^{86}Sr = 0.7056$ and Haroharo $^{87}Sr/^{86}Sr = 0.7054$) suggest similar magma sources and similar assimilation and fractional crystallization processes for the two complexes. Overall homogeneity of plagioclase (excluding relict cores) indicates no significant changes in contributions (i.e., crustal assimilation, mafic influx) to the system during the majority of plagioclase crystal growth. Furthermore, lack of $^{87}Sr/^{86}Sr$ ratio fluctuations in plagioclase rims suggest interaction between the resident silicic magma and the intruding mafic magma that triggered the eruptions was largely limited to volatile and heat transfer. Using appropriate standards and analysis, this MC-SIMS method can be used to detect short-lived, open-system events in magma reservoirs where differences in $^{87}Sr/^{86}Sr$ isotopic ratios are significant.

Keywords: Sr isotopes; SIMS; plagioclase; Okataina; rhyolite

1. Introduction

Analyses of micro-geochemical growth zones in individual crystals are used to understand the evolution of magmatic systems (e.g., Davidson et al., 2007, 1998; Ramos and Tepley, 2008). Crystal growth patterns are utilized to trace changes in intensive parameters (e.g., pressure, temperature, oxygen fugacity) and physio-chemical processes (e.g., fractionation, mixing) that magmas undergo as they ascend and stall in the Earth's crust before erupting at the surface. Plagioclase is one of the more frequently studied minerals because it is stable across a wide range of pressures, temperatures and H_2O contents, and responds readily to fluctuations in these conditions, ultimately providing a record of magmatic evolution (e.g., Ginibre et al., 2007; Ginibre and Davidson, 2014; Humphreys et al., 2006; Shane, 2015; Singer et al., 1995; Streck, 2008; Ustunisik et al., 2014). Plagioclase has been frequently used in petrologic studies over the last two decades, particularly with the development of techniques that permit micro-analysis of geochemical characteristics and Sr isotopic compositions in this mineral (e.g., Borges et al., 2014; Charlier et al., 2008; Christensen et al., 1995; Davidson et al., 2001; Font et al., 2008; Lange et al., 2013; Ramos et al., 2004; Takahashi et al., 2006; Tepley III et al., 2000). Coupling elemental and textural zoning with $^{87}Sr/^{86}Sr$ isotopic variations in plagioclase helps in determining the degree of crustal contamination of magmas and identifying the occurrence of magmatic recharge events.

Conventional techniques utilized to determine $^{87}Sr/^{86}Sr$ isotopic compositions in plagioclase include thermal ionization mass spectrometry (TIMS) and laser ablation multi-collector inductively-coupled plasma mass spectrometry (LA-MC-ICP-MS). TIMS is a high-precision technique (with typical 2σ uncertainties of ca. 0.000025 ± 10; e.g., Charlier et al., 2006; Gao et al., 2015; Kimura et al., 2013; Lange et al., 2013), but involves time-consuming sample preparation, including micromilling and chemical purification, which limits the number of samples that can be prepared. LA-MC-ICP-MS, in contrast, is an *in-situ* technique that allows for rapid analysis of crystals with relatively minimal sample preparation, but slightly lower precision and accuracy (2σ commonly 0.000080 ± 30; e.g., Burns et al., 2015; Coote et al., 2018; Gao et al., 2015). However, the ablation diameter needed to maintain the aforementioned precision is large, at least 50 μm and often ≥ 100 μm in cases of lower Sr concentrations (e.g., Andrews et al., 2008; Christensen et al., 1995; Coote et al., 2018; Davidson et al., 2001; Gao et al., 2015; Kimura et al., 2013; Ramos et al., 2004; Vroon et al.,

2008; Waight et al., 2002; Yang et al., 2013). This can result in analyses that cover more than one compositional domain (i.e., zone) within a crystal, which is also an issue for TIMS as microdrilling may result in removal of multiple compositional zones (minimum of 50 μm width and >> 100 μm in length; e.g., Chadwick et al., 2007; Charlier et al., 2008, 2006; Davidson and Tepley III, 1997; Font et al., 2008; Lange et al., 2013; Morgan et al., 2007; Takahashi et al., 2013). Furthermore, small plagioclase crystals (<50 μm) cannot currently be analysed *in-situ* (only via TIMS low blank chromatography; e.g., Ramos and Tepley III, 2008), and plagioclase crystals containing abundant micro-inclusions prove challenging to analyse. In an attempt to advance our understanding of magmatic processes and minimize issues surrounding averaging of compositional domains, small crystal size, and inclusion-rich crystals, we utilized a multi-collector secondary ion mass spectrometer (MC-SIMS) to obtain high resolution (~12 μm diameter) $^{87}Sr/^{86}Sr$ isotopic compositions in plagioclase. The ~12 μm spatial resolution of MC-SIMS for Sr isotopes is unobtainable by TIMS and LA-MC-ICP-MS since such small amounts of sample do not contain enough Sr for high-precision analysis (Charlier et al., 2006; Ramos and Tepley, 2008).

The ion microprobe allows for *in-situ* high resolution, high sensitivity analysis with spatial resolution on a micron scale and analytical precision better than 0.001 depending on the material and isotope species analysed (e.g., Budd et al., 2017; Kawasaki et al., 2017, 2015; Valley and Kita, 2009; Weber et al., 2005). Another advantageous aspect of SIMS is the ability to overcome many isobaric interferences through use of high mass resolving power ($M/\Delta M$). Ion microprobe analysis of Sr isotopes has been conducted (Exley, 1983; Kennedy et al., 1990; Sano et al., 2008; Scatena-Wachel, 1986; Weber et al., 2005), although previous studies have focused on carbonates (Table 1), particularly calcite, as it is compositionally simple and has high abundances of Sr yet low Rb/Sr (thus minimizing ^{87}Rb interferences on ^{87}Sr). Here we attempt to obtain accurate $^{87}Sr/^{86}Sr$ data of plagioclase, a compositionally more complex mineral with higher Rb/Sr ratios. In this study, instrument configuration, isobaric interferences, results, geochemical implications, and applicability of the ion microprobe as means for measuring Sr isotopic composition in plagioclase are discussed.

Table 1
Summary of previous $^{87}Sr/^{86}Sr$ ion microprobe studies

Instrument	Spot	Sample	Sr (ppm)	Max 2σ	M/ΔM	Study

	(μm)					
AEI-IM20	10	calcite	400	0.002	200	Exley (1983)
AEI-IM20	10	calcite	400	0.002	200	Scatena-Wachel (1986)
SHRIMP-RG	25	otolith	≤1500	0.002	7000-9000	Weber et al. (2005)
NanoSIMS NS50	5	otolith	<2000	0.003	3600	Sano et al. (2008)
IMS 1280HR	12	plagioclase	<1500*	0.0009	7000	This study

*Sr ppm for Kaharoa plagioclase from Shane (2015)

2. Okataina Volcanic Centre and sample selection

Plagioclase crystals used for this study were collected from the Okataina Volcanic Centre (OVC) in the Taupo Volcanic Zone (TVZ; Fig. 1). The TVZ is a NNE-SSW trending active volcanic arc in North Island, New Zealand, and is the on-land continuation of the Tonga-Kermadec arc, where volcanism is associated with subduction of the Pacific Plate beneath the Australian Plate (Stern, 1987). Formation of the TVZ started ca. 2 Ma ago with regular episodic volcanic activity resulting in total erupted volume $>10^4$ km^3, which is comparable to the Yellowstone system in North America, making it the most active Quaternary silicic system on Earth (Houghton et al., 1995; Wilson et al., 1984). The OVC is one of only two currently dormant rhyolite centres in the central TVZ, and of the two is the most recently active. Voluminous, regular activity at OVC began at ca. 625 ka and includes at least three caldera-forming events (Cole et al., 2014). Volcanism at OVC is bimodal with dominantly rhyolitic and minor basaltic erupted material (Nairn, 2002). Studies of rhyolitic deposits indicate that many OVC eruptions, both caldera-forming and intra-caldera, result from influx of hotter mafic magma into cooler, multi-level and laterally discontinuous silicic reservoirs (e.g., Leonard et al., 2002; Nairn et al., 2004, 2005, 2001; Shane, 2015; Shane et al., 2008; Storm et al., 2014, 2012, 2011).

There are two intra-caldera volcanic complexes at OVC with distinctive and parallel linear vent alignments, Tarawera to the south and Haroharo to the north. Eruptions at both complexes emanate from multiple vents along the length of their respective linear vent zones, a characteristic that is atypical for silicic eruptions and is thought to be controlled by regional extensional structures (Nairn, 2002). Selected units for analysis here include pumice from two recent post-caldera eruptions: (1) Kaharoa (0.7 ka), which erupted from the Tarawera Volcanic Complex, and (2) Rotoma (9.5 ka), which erupted from the Haroharo Volcanic

Complex (Nairn, 2002). Both units reflect typical post-50 ka OVC eruptive behaviour (i.e., explosive and effusive, simultaneous ejection from multiple vents, eruption of more than one magma composition; e.g., Shane et al., 2008, 2007; Smith et al., 2006). Their mineralogy (plagioclase+quartz >> Fe-Ti oxides > orthopyroxene+hornblende) is also typical of recently erupted magmas, although Kaharoa contains biotite and minor cummingtonite, whereas in Rotoma cummingtonite is a major ferromagnesian mineral and biotite is absent (any biotite in Rotoma is relict; Leonard et al., 2002; Nairn et al., 2004; Smith et al., 2005).

Kaharoa is the youngest rhyolitic eruption and the largest (~9 km^3) TVZ eruption in the last 1,000 years, with eruptive materials including both lavas and pyroclastics with SiO_2 = 75 – 77 wt% (Leonard et al., 2002; Nairn et al., 2004; Sahetapy-Engel et al., 2014). The Kaharoa magmatic system has been modelled as a stratified, sill-like (8 km x 1 km, >1 km in thickness) reservoir with three compositionally diverse and individually homogeneous rhyolitic magmas: (1) T1, the first to erupt, (2) T2, the last to erupt and with higher Zr and Sr relative to T1, and (3) T3, un-erupted rhyolite that mixed with basalt-derived residual melt (dacite) to produce erupted rhyodacites (Nairn et al., 2004). Kaharoa was specifically selected based on previous studies (Leonard et al., 2002; Nairn et al., 2004, 2001; Shane, 2015) that suggested multiple injections of basalt into the Kaharoa sill occurred before eruption. Plagioclase used for analysis was extracted from T2, because this unit shows greater evidence for interaction with basalt than T1, as well as representing the largest volumetric component of the Kaharoa magmatic system (Nairn et al., 2004).

Rotoma also erupted pyroclastics and lavas with high silica contents (SiO_2 = 75 – 78 wt%) and similar volume to Kaharoa (~8 km^3; Smith et al., 2006). Smith et al. (2006) interpreted the Rotoma magmatic system to be a storage system with separate, well-homogenised bodies of magma and multiple conduits. Two compositionally discrete magmas (RT1 and RT3) were tapped during the Rotoma eruption and hybridized in central vents to form a third unit (RT2). Smith et al., (2006) suggest that Rotoma rhyolites RT1 and RT3, unlike the Kaharoa rhyolites T1 and T2, were able to homogenise rather than mingle due to them having similar H_2O contents, densities and viscosities. Although Rotoma deposits show no evidence for interaction with basalt, mafic magma intrusion remains a possible cause for eruption because this process is common at the OVC. An alternative triggering mechanism could be seismic activity, as Rotoma deposits are found

directly above an earthquake rupture (Smith et al., 2006). Plagioclase crystals from unit RT2 were selected for analysis.

Additional criteria for unit selection included abundance (≥1%) and size (≥100 μm) of plagioclase crystals and availability of whole rock and mineral geochemistry data. Size criteria were set to test the accuracy of isotopic ratios using additional methods, which require large (≥100 μm) crystals. Approximately 300 plagioclase crystals from each unit were handpicked, mounted in 25 mm diameter epoxy plugs, and polished for microanalysis. Identification of compositional and textural characteristics were completed using electron backscatter imaging (BSE) and electron microprobe analysis (EPMA). Optimal crystals for isotopic microanalyses were selected based on crystal orientation, complete crystal stratigraphy from core to rim, and a good crystal surface (i.e., minimal scratches, cracks, and mineral or melt inclusions). A total of seven representative crystals were analysed from Kaharoa and five from Rotoma.

3. Analytical methods

3.1 Electron microprobe analysis

EMPA was completed to determine major and minor element concentrations of plagioclase and was done using a JEOL JXA-8230 SuperProbe at Victoria University of Wellington. EMPA analyses were done post-MC-SIMS, to match spot locations as closely as possible, and pre-LA-MC-ICP-MS. Elements analysed and their uncertainties are Si (1%), Ca (2%), Na (4%), K (7%), Al (1%), Mg (4%), and Fe (5%). The precision reported here is calculated using standard values collected during the analytical session. In effort to help reduce uncertainties, Mg and Fe had peak counting times of 90 s, whereas all other elements has peak counting times of 30 s. However, for concentrations close to the detection limit, such as Mg in plagioclase, uncertainties will be larger. Instrument conditions included an accelerating voltage of 15 kV, 1–2 μm beam size, and a 20 nA current. NMNH-115900 plagioclase was used as a standard.

3.2 Laser ablation multi-collector inductively-coupled plasma mass spectrometry analysis

MC-SIMS $^{87}Sr/^{86}Sr$ ratios measured in OVC plagioclase were compared to $^{87}Sr/^{86}Sr$ ratios obtained from LA-MC-ICP-MS. Analyses were done at the WM Keck Collaboratory for Plasma Mass Spectrometry at Oregon State University using a Nu Plasma MC-ICP-MS equipped with a Photon Machines G2 193nm ArF Excimer LA system. The carrier gas was He at flow rates of 0.3 L/min. Ablation troughs were 65–85 μm in diameter and 20–25 μm in depth (depth measured using a Keyence VK-X200 3D laser scanning microscope). Smaller ablation diameters were used in effort to analyse the same compositional domains (or as similar as possible) analysed by MC-SIMS. Laser analyses were done using a fluence of 4.84 J/cm^2 and pulse rates of 15 Hz for standards and 30 Hz for plagioclase. Troughs were analysed across samples at a rate of 5 μm/s. Measured masses were 83, 84, 85, 86, 87 and 88. On-peak corrections were made by measuring background values for Kr isotopes and other gas species introduced by the plasma prior to ablation of samples, then subtracting the background values from measured intensities. Corrections for mass bias were applied using measured $^{86}Sr/^{88}Sr = 0.1194$. Contributions from ^{87}Rb were corrected for by measuring ^{85}Rb intensity, and calculated ^{87}Rb contributions used the same mass bias as calculated for Sr isotopes. Previous studies have shown that contributions from Ca dimers and argides are negligible (Miller and Kent, 2009), therefore Ca species were not monitored. NIST 610 glass was used for tuning the instrument, and a modern gastropod ($^{87}Sr/^{86}Sr$ 0.709190 ± 0.000008; Miller and Kent, 2009) was used as an internal standard. A correction was applied to measured $^{87}Sr/^{86}Sr$ ratios in plagioclase based on small differences between the measured and accepted composition of the gastropod during the same analytical session (typically $\Delta^{87}Sr/^{86}Sr$ of 0.0002 to 0.0004; Miller and Kent, 2009). A secondary standard, a low-Rb, high-Sr clinopyroxene with homogeneous $^{87}Sr/^{86}Sr$ (0.704470 ± 0.000017 and 0.704482 ± 0.000010; Burns et al., 2015), was analysed as an unknown to further monitor instrument accuracy. The average $^{87}Sr/^{86}Sr$ value for the clinopyroxene standard throughout measurement was 0.70463 ± 0.00017. The average $^{84}Sr/^{86}Sr$ ratio measured of this standard was 0.0569 ± 0.0014.

Troughs were set up from core to rim of each crystal to measure $^{87}Sr/^{86}Sr$ compositional profiles similar to those obtained via MC-SIMS (see Section 3.3; e.g., Figs. 2 – 3). Plagioclase signals were divided and reduced into core, middle and rim bins, or into core and rim bins when the crystal was compositionally homogeneous and/or when more bins were not statistically viable. These bins were selected in an effort to

match the spatial resolution of MC-SIMS, as well as to track $^{87}Sr/^{86}Sr$ variations between zones with differing An contents. Reported uncertainties in LA-MC-ICP-MS $^{87}Sr/^{86}Sr$ ratios represent standard error (2se) calculated from repeat analysis of the measured $^{87}Sr/^{85}Sr$ ratios in the selected portion of each crystal, propagated quadratically with the standard error calculated from repeated analysis of the gastropod standard for that analytical session (to include both the within-run uncertainty and external uncertainty). To account for any inclusions sampled by the laser during ablation, signals showing ^{85}Rb spikes were excluded during the reduction process.

3.3 Secondary ion mass spectrometry analysis

Measurements of $^{87}Sr/^{86}Sr$ isotopic compositions in plagioclase were done using a CAMECA IMS 1280-HR located at Hokkaido University. An $^{16}O^-$ primary ion beam of 23 keV with a current of ~6 nA and a diameter of ~12 μm was used in the experiment. The mass resolution of $M/\Delta M$ was set at ~7,000 to maintain sub-per mille precision. While many interferences are eliminated through use of $M/\Delta M \geq 7{,}000$ (Weber et al., 2005), several Ca species are still potentially problematic, and isobaric interference of $^{87}Rb^+$ is unresolvable (respective $M/\Delta M$):

$^{87}Sr^+$: $^{87}Rb^+$ (300,000), $^{43}Ca^{44}Ca^+$ (16,200), $^{48}Ca^{39}K^+$ (11,800), $^{86}Sr^1H^+$ (10,600)

$^{86}Sr^+$: $^{42}Ca^{44}Ca^+$ (17,800), $^{40}Ca^{46}Ca^+$ (12,200), $^{43}Ca_2^+$ (10,400)

Therefore contributions of $^{87}Rb^+$ on $^{87}Sr^+$ were corrected based on secondary ion intensity of $^{85}Rb^+$ (Fig. A1; Table B1) assuming $^{85}Rb/^{87}Rb = 2.5926$ (Rosman and Taylor, 1998). Contributions of $^{42}Ca^{44}Ca^+$ on $^{86}Sr^+$ and $^{43}Ca^{44}Ca^+$ on $^{87}Sr^+$ were corrected based on $^{40}Ca_2^+$ and assuming that secondary ion intensities of the Ca dimers equal to Ca-isotope ratios of $^{40}Ca/^{42}Ca = 149.8145$, $^{40}Ca/^{43}Ca = 702.3913$, and $^{40}Ca/^{44}Ca = 46.3115$ (Rosman and Taylor, 1998), although the contributions of the Ca dimer ions were determined to be negligible in our analyses (Fig.A2; Table B1). Contributions of $^{86}Sr^1H^+$ were evaluated using $M/\Delta M$ = ca. 20,000 and deemed to be trivial (Fig. A2). Positive secondary ions ($^{85}Rb^+$, $^{86}Sr^+$, and $^{87}Sr^+$) were measured simultaneously in multi-collection mode using three electron multipliers (EMs). Obtained count rates were corrected for EM dead time and relative yield of each detector. Each measurement was conducted with 100 cycles of counting the secondary ions for 4 s. On spots analysed using multi-collection mode, $^{40}Ca_2^+$ was subsequently measured

with 10 cycles of counting for 4 s using an EM by the peak-jumping of a sector magnet. Plagioclase (anorthite, An_{97-94}, mounted and polished) from Miyakejima volcano, Japan, with homogeneous $^{87}Sr/^{86}Sr$ (0.70345; Arakawa et al., 1992; Kimura et al., 2013) was used as a calibration standard to normalize differences in the relative yield of detectors between each analytical session with average external reproducibility of 0.0007 (2σ). Approximately 35% of analyses comprised of standard measurements.

4. Results

4.1 Plagioclase composition and textures

Major and minor element concentrations of plagioclase are summarized in Table B2. Plagioclase An contents are similar across the two Okataina units, and the majority of crystals exhibit normal zoning. Kaharoa plagioclase is in the range An_{20-43} with few An_{60-71} cores. Rotoma plagioclase is in the range An_{29-43} with few calcic cores or compositional zones with An_{48-65}. Contents of FeO in all plagioclase crystals mimic An compositional patterns (decrease with lower An). Plagioclase crystals from the two units also have resorbed cores that are either more or less calcic than their respective rim. Calcic cores have either a sharp (Fig. 2) or gradational (Fig. 3C) boundary with sodic rims, whereas sodic cores are rounded (and often frayed-looking; Fig. 3B) with calcic rims. In both units, the differences in An contents between sodic cores and calcic rims are lesser than between calcic cores and sodic rims. Several Kaharoa crystals exhibit boxy-cellular core textures (Fig. 3A) that resemble chess boards, as noted by Shane (2015). Rotoma crystals rarely exhibit boxy-cellular textures, but several crystals have distinct zones (≤80 μm in width) between the core and rim that are dominated by inclusions (Fig. 3C).

4.2 LA-MC-ICP-MS analyses

Inter- and intra-crystal Sr isotopic compositions of plagioclase are commonly homogeneous within error based on LA-MC-ICP-MS analysis. LA-MC-ICP-MS results are summarized in Figure 4 and listed in Table 2. Kaharoa (Figs. 2 – 3 and 5) and Rotoma (Figs. 3 and 6) crystals cluster within the same $^{87}Sr/^{86}Sr$ range. Plagioclase crystals analysed in this study show no clear correlation between An contents and Sr isotopic compositions.

Table 2
LA-MC-ICP-MS analyses of OVC plagioclase

Plagioclase	Bin	$^{87}Sr/^{86}Sr$	2se	Plagioclase	Bin	$^{87}Sr/^{86}Sr$	2se
Kaharoa				*Rotoma*			
KA2-1	core	0.70547	0.00030	RM1-1	core	0.70534	0.00026
	mid	0.70538	0.00015		mid	0.70528	0.00016
KA2-2	core	0.70552	0.00019		rim	0.70540	0.00028
	rim	0.70574	0.00025	RM1-2	core	0.70583	0.00027
KA2-3	core	0.70635	0.00038		rim	0.70558	0.00018
	mid	0.70602	0.00081	RM1-5	core	0.70569	0.00033
	rim	0.70537	0.00046		mid	0.70556	0.00020
KA2-4	mid	0.70549	0.00022		rim	0.70569	0.00025
	rim	0.70526	0.00034	RM2-1	core	0.70597	0.00035
KA3-1	core	0.70549	0.00028		mid	0.70570	0.00019
	mid	0.70534	0.00023		rim	0.70559	0.00018
	rim	0.70589	0.00033	RM3-1	core	0.70580	0.00032
KA3-2	core	0.70590	0.00047		mid	0.70569	0.00017
	rim	0.70581	0.00021		band	0.70593	0.00026
KA3-6	core	0.70550	0.00041		rim	0.70570	0.00022
	mid	0.70558	0.00022				
	rim	0.70568	0.00043				

4.3 MC-SIMS analyses

Raw MC-SIMS data (corrected for $^{87}Rb^{+}$ and Ca dimers, see Section 3.3) were corrected in two steps: (1) An instrumental mass fractionation (IMF) correction was applied (annotated as $^{87}Sr^{+}/^{86}Sr^{+}_{SIMS}$ in the equation below). Raw and IMF-corrected $^{87}Sr^{+}/^{86}Sr^{+}$ ratios are listed in Table B1. (2) A matrix effect correction was made, because MC-SIMS data show a broad correlation between SIMS $^{87}Sr^{+}/^{86}Sr^{+}$ secondary ion intensity ratios and plagioclase An contents (Fig. 7). The complexity of plagioclase, a solid solution series of Ca-Na feldspar minerals, makes it a likely candidate for an analytical matrix effect – a well-known issue with SIMS analysis (e.g., Eiler et al., 1997). Figure 7 specifically shows that higher An zones yield higher $^{87}Sr^{+}/^{86}Sr^{+}$ ion count ratios; a pattern that was not observed in data acquired via LA-MC-ICP-MS.

Since the Sr isotopic ratios obtained by LA-MC-ICP-MS yielded constant $^{87}Sr/^{86}Sr$ ratios for zones with uniform An contents, the observed matrix effects for SIMS data can be corrected using these LA-MC-ICP-MS data. The correction was conducted using the following equation:

$$\frac{^{87}Sr}{^{86}Sr}_{final} = \left[\left(\frac{^{87}Sr^{+}}{^{86}Sr^{+}}_{SIMS}\right) - (m \times An\ content) - \left(y - \frac{^{87}Sr}{^{86}Sr}_{LA-MC-ICP-MS}\right)\right]$$

The LA-MC-ICP-MS $^{87}Sr/^{86}Sr$ ratio used for calculations is 0.70561 ± 0.00045, and it represents the average LA-MC-ICP-MS value. Variables *m* and *y* represent the slope ($4.06\times10^{-5} \pm 0.78\times10^{-5}$) and y-intercept (0.70669 ± 0.00029), respectively, calculated using the ISOPLOT (Ludwig, 2003) linear regression model 1 for all SIMS $^{87}Sr^{+}/^{86}Sr^{+}$ ion intensity ratios versus An contents (Fig. 7). We propagated the uncertainties of the repeated measurements of the Miyakejima anorthite standard, the LA-MC-ICP-MS data (2SD), and the slope and intercept of the regression, to obtain a combined precision of about ± 0.0008 (2σ) for our MC-SIMS analyses. Final, matrix effect-corrected $^{87}Sr/^{86}Sr$ ratios are listed in Table 3.

Following matrix effect correction, the Sr isotopic ratios obtained via MC-SIMS are in agreement with Sr isotopic ratios obtained through LA-MC-ICP-MS for the same crystal compositional domains within the errors. Thus, we successfully measured $^{87}Sr/^{86}Sr$ ratios for the plagioclase crystals with ± 0.0008 precision and ~12 μm spatial resolutions by MC-SIMS.

Table 3
Final corrected MC-SIMS analyses.

Plagioclase	Spot No.*	An	$^{87}Sr/^{86}Sr$	2σ	Plagioclase	Spot No.*	An	$^{87}Sr/^{86}Sr$	2σ
Kaharoa					*Kaharoa continued*				
KA2-1	37	39	0.7057	0.0008		210	24	0.7059	0.0008
	39	43	0.7051	0.0008		211	24	0.7055	0.0008
	40	38	0.7050	0.0008		212	21	0.7053	0.0008
	43	31	0.7055	0.0008	KA3-6	215	33	0.7057	0.0008
	44	36	0.7058	0.0008		336	33	0.7051	0.0008
	46	32	0.7056	0.0008		216	32	0.7056	0.0008
	48	21	0.7061	0.0008		337	32	0.7045	0.0008
KA2-2	49	71	0.7055	0.0009		340	32	0.7051	0.0008
	56	71	0.7056	0.0009		217	31	0.7055	0.0008
	128	67	0.7053	0.0009		223	28	0.7058	0.0008
	50	62	0.7059	0.0009		218	28	0.7062	0.0008
	132	62	0.7056	0.0009		338	28	0.7054	0.0008
	51	31	0.7055	0.0008		221	22	0.7055	0.0008
	129	31	0.7054	0.0008		219	22	0.7055	0.0008
	57	31	0.7058	0.0008		220	20	0.7050	0.0007
	131	28	0.7060	0.0008		222	20	0.7051	0.0007
	133	31	0.7056	0.0008	*Rotoma*				
	81	39	0.7055	0.0008	RM1-1	384	65	0.7039	0.0009
	52	29	0.7060	0.0008		385	58	0.7047	0.0009
	59	29	0.7057	0.0008		392	58	0.7045	0.0009
	84	31	0.7058	0.0008		386	51	0.7048	0.0008
	83	31	0.7060	0.0008		391	31	0.7056	0.0008
	86	31	0.7060	0.0008		387	43	0.7053	0.0008
	53	31	0.7065	0.0008		388	31	0.7055	0.0008
	88	25	0.7053	0.0008		390	31	0.7051	0.0008
	130	25	0.7059	0.0008		389	30	0.7054	0.0008

	85	25	0.7061	0.0008	RM1-2	403	52	0.7055	0.0008
KA2-3	135	60	0.7069	0.0009		404	53	0.7050	0.0008
	136	58	0.7071	0.0009		405	48	0.7052	0.0008
	137	58	0.7070	0.0009		406	37	0.7054	0.0008
	138	30	0.7065	0.0008		408	40	0.7056	0.0008
	134	34	0.7059	0.0008		409	37	0.7056	0.0008
	139	34	0.7055	0.0008	RM1-5	418	49	0.7058	0.0008
	140	29	0.7059	0.0008		419	36	0.7058	0.0008
	141	24	0.7060	0.0008		420	40	0.7058	0.0008
	142	26	0.7062	0.0008		421	35	0.7055	0.0008
	143	23	0.7062	0.0008		422	34	0.7059	0.0008
KA2-4	145	33	0.7055	0.0008		423	34	0.7059	0.0008
	146	38	0.7059	0.0008		424	34	0.7061	0.0008
	147	40	0.7062	0.0008		425	31	0.7057	0.0008
	148	34	0.7059	0.0008		426	31	0.7051	0.0008
	149	25	0.7059	0.0008		427	38	0.7052	0.0008
	203	25	0.7051	0.0008		428	49	0.7062	0.0008
	144	25	0.7063	0.0008		429	40	0.7056	0.0008
	150	26	0.7062	0.0008		430	37	0.7051	0.0008
	151	21	0.7052	0.0008	RM2-1	368	35	0.7045	0.0008
	152	21	0.7056	0.0008		369	30	0.7059	0.0008
	202	21	0.7043	0.0008		370	39	0.7055	0.0008
KA3-1	243	37	0.7060	0.0008		371	29	0.7056	0.0008
	244	38	0.7065	0.0008		372	36	0.7054	0.0008
	245	61	0.7058	0.0009		373	31	0.7054	0.0008
	246	53	0.7060	0.0008		374	31	0.7056	0.0008
	247	36	0.7057	0.0008		375	30	0.7052	0.0008
	248	33	0.7063	0.0008	RM3-1	346	29	0.7057	0.0008
	249	27	0.7058	0.0008		347	29	0.7058	0.0008
	250	21	0.7047	0.0007		348	34	0.7060	0.0008
KA3-2	214	26	0.7052	0.0008		349	34	0.7061	0.0008
	205	26	0.7056	0.0008		350	34	0.7059	0.0008
	206	26	0.7053	0.0008		351	32	0.7058	0.0008
	213	26	0.7051	0.0008		352	33	0.7056	0.0008
	207	25	0.7051	0.0008		353	41	0.7056	0.0008
	208	31	0.7058	0.0008		354	35	0.7059	0.0008
	209	33	0.7056	0.0008		355	38	0.7056	0.0008
	204	33	0.7053	0.0008		356	38	0.7051	0.0008

*SIMS spots are listed in order from core to rim.

5. Discussion

5.1 Implications for using the MC-SIMS technique

MC-SIMS is potentially valuable for deciphering magmatic processes at higher spatial resolutions. The precision (± 0.0008) of the MC-SIMS method may be inadequate to identify variations in large, buffered magmatic systems in continental settings or mid-ocean ridge volcanoes, where isotopic fluctuations are slight

(e.g., Lange et al., 2013; Wolff et al., 1999; Table 4). However, many studies that investigate isotopic fluctuations in volcanic crystals extracted from rocks from subduction zones, flood basalts, and intra-plate basalts reveal isotopic heterogeneities greater than the average MC-SIMS error (e.g., Alves et al., 2009; Borges et al., 2014; Burns et al., 2015; Charlier et al., 2008; Coote et al., 2018; Davidson et al., 2001; Font et al., 2008; Gao et al., 2015; Tepley III et al., 2000; Yang et al., 2013; Table 4). The ion microprobe therefore allows for *in-situ* Sr isotopic analysis and minimal sample preparation relative to TIMS, and offers a spatial resolution that is five to ten times greater than that of LA-MC-ICP-MS.

5.2 Sr diffusion in OVC plagioclase?

Sr diffusion may have dampened any original $^{87}Sr/^{86}Sr$ variations that may have been present in OVC plagioclase. Diffusion of Sr is more rapid in sodic than in calcic plagioclase. At a temperature range of 724 – 760˚C (Nairn et al., 2004; Smith et al., 2006), and an An range of 20 – 43, diffusion coefficients range from 1.4×10^{-19} to 5.0×10^{-21} m^2 s^{-1} (Giletti and Casserly, 1994). To provide a maximum timescale for diffusion to equilibrate potential initial $^{87}Sr/^{86}Sr$ variations, we can use the approach of Zellmer et al. (1999) and assume an initial step starting profile with relative variations in ^{87}Sr and ^{86}Sr concentrations, i.e., variable $^{87}Sr/^{86}Sr$ ratios, and with a step width of 70 μm (equivalent to the average spacing of the analyses undertaken in this study). In this scenario, any isotopic variations would decay to 10% of their initial values between ca. 300 yrs (760˚C, An_{20}) and ca. 8,000 yrs (724˚C, An_{43}). However, Shane (2015) analysed numerous Kaharoa plagioclase crystals for major, minor and trace element compositions, and showed that Sr concentration profiles mimic An trends in Kaharoa plagioclase (i.e., increasing with An contents). This observation is inconsistent with any progressed degree of Sr elemental diffusion, which would result in Sr profiles that mirror An trends (e.g., Bindeman et al., 1998; Dohmen et al., 2017; Zellmer et al., 1999). Therefore, we consider their Sr isotopic uniformity to be a reflection of a primary petrogenetic characteristic, rather than a result of diffusive equilibration.

5.3 Comments on the OVC system

For MC-SIMS analyses of Kaharoa and Rotoma plagioclase crystals that have uniform An contents, we infer homogeneous Sr isotopic compositions to a high spatial resolution (12 μm) in individual crystals.

Table 4

Summary table of previously reported $^{87}Sr/^{86}Sr$ ratios in magmatic plagioclase ($CaAl2Si_2O_8$ to $NaAlSi_3O_8$).

Study	Method[a]	Sample location	$^{87}Sr/^{86}Sr$ maximum	$^{87}Sr/^{86}Sr$ minimum	$^{87}Sr/^{86}Sr$ Δ[b]	Precision[c]		Size[d]
Alves et al., (2009)	LA	Maua Granite Pluton, Brazil	0.71540	0.71040	0.0050	0.00070	2σ	160 (μm-d)
Arakawa et al., (1992)	TIMS	Miyakejima Volcano, Japan	0.70351	0.70341	*0.0001*	0.00002	2σ	(whole)
Borges et al., (2014)	LA	Deccan Traps, India	0.71061	0.70968	0.0009	0.00016	2se	80 (μm-d)
Burns et al., (2015)	LA	Purico-Chascón Volcanic Complex, Chile	0.70900	0.70570	0.0033	0.00180	2se	65 (μm-d)
--	TIMS	Purico-Chascón Volcanic Complex, Chile	0.70890	0.70880	0.0001	0.00002	2se	65 (μm-w)
Chadwick et al., (2007)	TIMS	Merapi Volcano, Java, Indonesia	0.70628	0.70577	0.0005	0.00002	2σ	≥50 (μm-w)
Charlier et al., (2006)	TIMS	Parinacota Volcano, Chile	0.70690	0.70670	0.0002	0.00006	2se	≥50 (μm-w)
Charlier et al., (2007)	TIMS	Fish Canyon Tuff, Colorado, USA	0.70670	0.70630	0.0004	0.00002	2σ	≥50 (μm-w)
Charlier et al., (2008)	TIMS	Oranui/Taupo Caldera, New Zealand	0.70764	0.70553	0.0021	0.00006	2σ	≤300 (μm-d)
Christensen et al., (1995)	LA	Long Valley, California, USA	0.70629	0.70595	0.0003	0.00005	2σ	130 (μm-d)
Coote et al., (2018)	LA	Kaikohe-Bay of Islands, New Zealand	0.70580	0.70320	0.0026	0.00008	2σ	500 (μm-w)
Davidson and Tepley III (1997)	TIMS	Chaos Crags, California, USA	0.704100	0.703700	0.0004	0.000005	2σ	500 (μm-w)
--	TIMS	Purico-Chascón Volcanic Complex, Chile	0.709200	0.706200	0.0030	0.000005	2σ	500 (μm-w)
--	TIMS	El Chichón Volcano, Mexico	0.705400	0.704500	0.0009	0.000005	2σ	≤300 (μm-d)
Davidson et al., (2001)	LA	El Chichón Volcano, Mexico	0.70630	0.70370	0.0026	0.00034	2σ	3-600 (ng)
Feldstein et al., (1994)	TIMS	San Vincenzo, Tuscany, Italy	0.71441	0.71355	0.0009	0.00005	2se	500 (μm-w)
Font et al., (2008)	TIMS	Skye Flood Basalts, UK	0.70530	0.70336	0.0019	0.00001	2σ	190 (μm-d)
Gao et al., (2015)	LA	Tengchong Volcanic Field, China	0.71380	0.70600	0.0078	0.00240	2σ	≥80 (μm-w)
Ginibre and Davidson (2014)	TIMS	Parinacota Volcano, Chile	0.70677	0.70659	0.0002	0.00003	2se	200 (μm-d)
Halama et al., (2002)	ICP-MS	Gardar Province, Greenland	0.70568	0.70369	0.0020	0.00011	2se	<1000 (μm-w)
Kimura et al., (2013)	LA	Azuma Volcano, Japan	0.70474	0.70461	0.0001	0.00010	2se	10-20 (ng)
Lange et al., (2013)	TIMS	Various mid-ocean ridge basalts (MORB)	0.70374	0.70338	0.0004	0.00005	2σ	≥50 (μm-w)
Morgan et al., (2007)	TIMS	Stromboli Volcano, Italy	0.70648	0.70617	0.0003	0.00002	2σ	≥50 (μm-w)
Ramos and Reid, (2005)	TIMS	Pisgah Cinder Cone, California, USA	0.70454	0.70429	0.0003	0.00001	2se	100 (ng)
Ramos et al., (2005)	LA	Columbia River Flood Basalts, USA	0.71277	0.71184	0.0009	0.00008	2se	≤160 (μm-d)
Ramos et al., (2004)	LA	Pisgah Cinder Cone, California, USA	0.70457	0.70429	0.0003	0.00009	2se	≤160 (μm-d)
Salisbury et al., (2008)	LA	Lassen Volcano, California, USA	0.70440	0.70398	0.0004	0.00018	2se	≤160 (μm-d)
Takahashi et al., (2013)	TIMS	Azuma Volcano, Japan	0.704712	0.704266	*0.0004*	0.000009	2σ	300 (μm-w)
--	LA	Azuma Volcano, Japan	0.70456	0.70394	0.0006	0.00005	2se	200 (μm-d)
Takahashi et al., (2006)	TIMS	Zao Volcano, Japan	0.70425	0.70420	0.00005	0.00002	2σ	7 (ng)

Tepley III and Davidson (2003)	TIMS	Rum Layered Intrusion, Scotland	0.70518	0.70454	0.0006	0.00003	2σ	200 (μm-w)
Tepley III et al., (1999)	TIMS	Chaos Crags, California, USA	0.70501	0.70378	0.0012	0.00007	2σ	≤800 (μm-w)
Tepley III et al., (2000)	TIMS	El Chichon Volcano, Mexico	0.70522	0.70421	0.0010	0.00002	2σ	500 (μm-w)
Waight et al., (2002)	LA	Gardiner Intrusion, Greenland	0.70383	0.70373	0.0001	0.00002	2se	≤200 (μm-d)
T. E. Waight et al., (2000)	ICP-MS	Lachlan Fold Belt, Australia	0.71163	0.70492	0.0067	0.00004	2σ	<900 (μm-w)
Tod E. Waight et al., (2000)	ICP-MS	Lachlan Fold Belt, Australia	0.73276	0.73020	0.0026	0.00003	2σ	<900 (μm-w)
Yang et al., (2013)	LA	Bushveld Complex, South Africa	0.70666	0.70506	0.0016	0.00042	2σ	≤200 (μm-d)

[a]LA refers to LA-MC-ICP-MS; ICP-MS refers to solution MC-ICP-MS.

[b]Variations in $^{87}Sr/^{86}Sr$ ratios represent single-crystal isotopic variations. If single-crystal variations were not available, ratios have been *italicized*.

[c]Precision listed in table is the lowest reported in the respective publication, or average if only average precision was reported.

This implies that An contents and Sr isotope ratios did not fluctuate dramatically during growth of these OVC crystals, and that open-system processes also did not vary significantly during the 9 ka interval between eruption of the two magmas studied. Previous investigations of recent, post-caldera OVC eruptions demonstrate that the intrusion of mafic magma, as evidenced by reversely zoned crystals and the presence of olivine and basaltic glass, triggered many of these eruptions, although pre-eruption interaction between rhyolites and basalts is limited due to the small volume of the intruder (e.g., Shane, 2015; Shane et al., 2008, 2007; Smith et al., 2004). Rims of plagioclase crystals analysed in this study reveal overall homogeneity, both isotopically ($^{87}Sr/^{86}Sr = 0.7056 \pm 0.0001$ among all analysed rims) and compositionally ($An_{30 \pm 7}$), and no evidence for interaction with mafic melts shortly prior to eruption. It may be that these crystals are not representative of the whole system. Since all analysed plagioclase crystals have rims that are normally-zoned and nearly identical in An contents, they may instead represent a portion of the system that is a buffered crystal mush, as has been suggested previously for Okataina and other felsic centres (Bachmann and Bergantz, 2004, 2008a, 2008b; Hildreth, 2004; Klemetti et al., 2011; Smith et al., 2005; Storm et al., 2012; Wilson and Charlier, 2016). However, it is also possible that the lack of An and isotopic variation along the rims of the plagioclase crystals implies more limited mixing between the intruder and resident magma than previously suggested.

The potential of basaltic intrusions serving as the primary trigger for eruption is especially pertinent for Kaharoa. Previous studies (Leonard et al., 2002; Nairn et al., 2004) suggest that multiple injections of primitive magma interacted with the silicic Kaharoa system prior to eruption. These studies suggested that the Kaharoa magma chamber was stratified, with three geochemically discrete rhyolitic magmas, which resulted in basalt intermingling with a limited part of the system (one magma situated at the base). Kaharoa plagioclase crystals analysed for isotopes were extracted from a unit interpreted to be isolated from the basalt injection until eruption (see Section 2). If these crystals do represent a buffered portion of the magma system, then Sr isotopic ratios are consistent with the aforementioned model where basalt interaction with the buffered portion of the system did not occur during plagioclase crystal growth. This supports a model where rejuvenation is mostly the product of heat and volatile transfer (e.g., Storm et al., 2014, 2012). Shane (2015) examined plagioclase from the same Kaharoa unit and observed greater textural and compositional variety among

crystals than found in this study, although rims also displayed low-An normal zoning consistent with crystallization in a buffered, cool magmatic system. Notably, crystals with higher-An cores are present and could be derived from a basaltic component (Leonard et al., 2002; Shane, 2015). If these remnant cores are derived from injecting basalt, any interaction between the buffered rhyolitic systems and the basalt was minimal and allowed the system to return to equilibrium well before eruption. Alternatively, the compositional and isotopic uniformity of plagioclase rims suggest these cores may be relict (Shane, 2015).

Rotoma eruptives, like Kaharoa, exhibit mixing between two compositionally varied rhyolites (Smith et al., 2006, 2005). Specifically, Smith et al. (2006) present geochemical evidence for two individually homogeneous rhyolitic magmas that erupted and mixed to form a hybrid erupted unit. However, the authors point out that there is no geochemical indication for basalt influx and no petrographic evidence for mingling of Rotoma rhyolite magmas with mafic liquids, which is supported by plagioclase Sr isotopic ratios. The Rotoma eruption differs further from Kaharoa in that spatial evidence suggests that the two magmas were stored separately, with vents covering a length of 12 km (Smith et al., 2006). The lateral extent of the Rotoma eruption, tapping of two separately-stored magmas, and previous studies suggesting earthquakes and eruptions are linked at OVC (Berryman et al., 2008), imply that seismic activity could also be a potential trigger. Nonetheless, the ability of rhyolitic systems to remain active is dependent on system rejuvenation through addition of high-temperature mafic magma, and studies illustrate this is an especially important process at OVC (e.g., Nairn et al., 2004; Shane et al., 2008, 2007; Smith et al., 2004; Storm et al., 2014, 2012, 2011). However, lack of compositional and Sr isotopic variability in Rotoma plagioclase crystals imply that, if reactivation resulted from mafic influx, it was dominantly driven by heat and volatile transfer rather than mass (liquid) transfer between basalts and rhyolites.

Kaharoa and Rotoma plagioclase Sr isotopic compositions support similar sources for the Tarawera and Haroharo volcanic complexes, despite evidence for a complex system of magma storage and conduits at OVC, and regardless of their observed mineralogical differences (e.g., biotite in Kaharoa, cummingtonite in Rotoma; Leonard et al., 2002; Shane, 2015; Shane et al., 2007; Smith et al., 2006, 2005). Measured $^{87}Sr/^{86}Sr$ ratios fall between two isotopic endmembers – the Mesozoic metasedimentary Waipapa and Torlesse Composite Terranes and mantle-derived basalt (Gamble et al., 1993; Graham and Cole, 1991; McCulloch et

al., 1994; Price et al., 2015). Specifically, these intermediate Sr isotope ratios indicate similar degrees of assimilation of metasediments with basalt (Smith et al., 2010, 2005). In addition, isotopic contrasts are subdued because the source for Mesozoic terranes are volcanic rocks and volcaniclastic materials from an arc environment (Price et al., 2015).

6. Conclusions

MC-SIMS allows for high-spatial resolution analysis of Sr isotopic compositions in plagioclase. Notably, the analytical uncertainty ca. ± 0.0008 of MC-SIMS makes this technique suitable for systems where $^{87}Sr/^{86}Sr$ isotopic variations at an intra-crystalline level are large (>0.001). In such cases, fluctuations can be identified to significantly higher spatial resolution than previously possible. Sr isotopic analyses of young OVC plagioclase support an origin from similar sources for the two intra-caldera volcanic complexes, Tarawera and Haroharo. Furthermore, plagioclase compositional and isotopic ratios are consistent with contributions from mafic inputs, which have been shown to trigger eruptions at OVC, are likely dominated by heating and gas fluxing rather than mass transfer.

Acknowledgements

Support for this project came from the New Zealand Ministry of Business, Innovation, and Employment grant MAUX1507 to GFZ, the University of Auckland Postgraduate Research Student Support award to MS, and by Monka-sho grants to NK and HY.

Appendices A and B. Supplementary data

Supplementary data associated with this article can be found at

References

Alves, A., de Assis Janasi, V., Simonetti, A., Heaman, L.M., 2009. Microgranitic Enclaves as Products of Self-mixing Events: a Study of Open-system Processes in the Maua Granite, Sao Paulo, Brazil, Based on in situ Isotopic and Trace Elements in Plagioclase. J. Petrol. 50, 2221–2247. https://doi.org/10.1093/petrology/egp074

Andrews, B.J., Gardner, J.E., Housh, T.B., 2008. Repeated recharge, assimilation, and hybridization in magmas erupted from El Chichón as recorded by plagioclase and amphibole phenocrysts. J. Volcanol. Geotherm. Res. 175, 415–426. https://doi.org/10.1016/j.jvolgeores.2008.02.017

Arakawa, Y., Murakami, H., Kimata, M., Shimoda, S., 1992. Strontium isotope compositions of anorthite and olivine phenocrysts in basaltic lavas and scorias of Miyakejima volcano, Japan. J. Mineral. Petrol. Econ. Geol. 87, 226–239.

Bachmann, O., Bergantz, G.W., 2008a. The magma reservoirs that feed supereruptions. Elements 4, 17–21. https://doi.org/10.2113/GSELEMENTS.4.1.17

Bachmann, O., Bergantz, G.W., 2008b. Rhyolites and their Source Mushes across Tectonic Settings. J. Petrol. 49, 2277–2285. https://doi.org/10.1093/petrology/egn068

Bachmann, O., Bergantz, G.W., 2004. On the Origin of Crystal-poor Rhyolites: Extracted from Batholithic Crystal Mushes. J. Petrol. 45, 1565–1582. https://doi.org/10.1093/petrology/egh019

Berryman, K., Villamor, P., Nairn, I., van Dissen, R., Begg, J., Lee, J., 2008. Late Pleistocene surface rupture history of the Paeroa Fault, Taupo Rift, New Zealand. N. Z. J. Geol. Geophys. 51, 135–158. https://doi.org/10.1080/00288300809509855

Bindeman, I.N., Davis, A.M., Drake, M.J., 1998. Ion microprobe study of plagioclase-basalt partition experiments at natural concentration levels of trace elements. Geochim. Cosmochim. Acta 62, 1175–1193. https://doi.org/DOI: 10.1016/S0016-7037(98)00047-7

Borges, M.R., Sen, G., Hart, G.L., Wolff, J.A., Chandrasekharam, D., 2014. Plagioclase as recorder of magma chamber processes in the Deccan Traps: Sr-isotope zoning and implications for Deccan eruptive event. J. Asian Earth Sci. 84, 95–101. https://doi.org/10.1016/j.jseaes.2013.10.034

Budd, D.A., Troll, V.R., Deegan, F.M., Jolis, E.M., Smith, V.C., Whitehouse, M.J., Harris, C., Freda, C., Hilton, D.R., Halldórsson, S.A., Bindeman, I.N., 2017. Magma reservoir dynamics at Toba caldera, Indonesia, recorded by oxygen isotope zoning in quartz. Sci. Rep. 7, 40624. https://doi.org/10.1038/srep40624

Burns, D.H., de Silva, S.L., Tepley, F., Schmitt, A.K., Loewen, M.W., 2015. Recording the transition from flare-up to steady-state arc magmatism at the Purico–Chascon volcanic complex, northern Chile. Earth Planet. Sci. Lett. 422, 75–86. https://doi.org/10.1016/j.epsl.2015.04.002

Chadwick, J.P., Troll, V.R., Ginibre, C., Morgan, D., Gertisser, R., Waight, T.E., Davidson, J.P., 2007. Carbonate Assimilation at Merapi Volcano, Java, Indonesia: Insights from Crystal Isotope Stratigraphy. J. Petrol. 48, 1793–1812. https://doi.org/10.1093/petrology/egm038

Charlier, B.L.A., Bachmann, O., Davidson, J.P., Dungan, M.A., Morgan, D.J., 2007. The Upper Crustal Evolution of a Large Silicic Magma Body: Evidence from Crystal-scale Rb–Sr Isotopic Heterogeneities in the Fish Canyon Magmatic System, Colorado. J. Petrol. 48, 1875–1894. https://doi.org/10.1093/petrology/egm043

Charlier, B.L.A., Ginibre, C., Morgan, D., Nowell, G.M., Pearson, D.G., Davidson, J.P., Ottley, C.J., 2006. Methods for the microsampling and high-precision analysis of strontium and rubidium isotopes at single crystal scale for petrological and geochronological applications. Chem. Geol. 232, 114–133. https://doi.org/10.1016/j.chemgeo.2006.02.015

Charlier, B.L.A., Wilson, C.J.N., Davidson, J.P., 2008. Rapid open-system assembly of a large silicic magma body: time-resolved evidence from cored plagioclase crystals in the Oruanui eruption deposits, New Zealand. Contrib. Mineral. Petrol. 156, 799–813. https://doi.org/10.1007/s00410-008-0316-y

Christensen, J.N., Halliday, A.N., Lee, D.-C., Hall, C.M., 1995. In situ Sr isotopic analysis by laser ablation. Earth Planet. Sci. Lett. 136, 79–85.

Cole, J.W., Deering, C.D., Burt, R.M., Sewell, S., Shane, P.A.R., Matthews, N.E., 2014. Okataina Volcanic Centre, Taupo Volcanic Zone, New Zealand: A review of volcanism and synchronous pluton development in an active, dominantly silicic caldera system. Earth-Sci. Rev. 128, 1–17. https://doi.org/10.1016/j.earscirev.2013.10.008

Coote, A., Shane, P., Stirling, C., Reid, M., 2018. The origin of plagioclase phenocrysts in basalts from continental monogenetic volcanoes of the Kaikohe-Bay of Islands field, New Zealand: implications for magmatic assembly and ascent. Contrib. Mineral. Petrol. 173. https://doi.org/10.1007/s00410-018-1440-y

Davidson, J., Tepley III, F.J., Palacz, Z., Meffan-Main, S., 2001. Magma recharge, contamination and residence times revealed by in situ laser ablation isotopic analysis of feldspar in volcanic rocks. Earth Planet. Sci. Lett. 184, 427–442.

Davidson, J.P., Morgan, D.J., Charlier, B.L.A., Harlou, R., Hora, J.M., 2007. Microsampling and Isotopic Analysis of Igneous Rocks: Implications for the Study of Magmatic Systems. Annu. Rev. Earth Planet. Sci. 35, 273–311. https://doi.org/10.1146/annurev.earth.35.031306.140211

Davidson, J.P., Tepley III, F.J., 1997. Recharge in Volcanic Systems: Evidence from Isotope Profiles of Phenocrysts. Science 275, 826–829.
Davidson, J.P., Tepley III, F.J., Knesel, K.M., 1998. Crystal isotope stratigraphy; a method for constraining magma differentiation pathways. Eos 79, 185–189.
Dohmen, R., Faak, K., Blundy, J.D., 2017. Chronometry and Speedometry of Magmatic Processes using Chemical Diffusion in Olivine, Plagioclase and Pyroxenes. Rev. Mineral. Geochem. 83, 535–575. https://doi.org/10.2138/rmg.2017.83.16
Eiler, J.M., Graham, C., Valley, J.W., 1997. SIMS analysis of oxygen isotopes: matrix effects in complex minerals and glasses. Chem. Geol. 138, 221–244.
Exley, R.A., 1983. Evaluation and application of the ion microprobe in the strontium isotope geochemistry of carbonates. Earth Planet. Sci. Lett. 65, 303–310.
Feldstein, S.., Halliday, A.., Davies, G.., Hall, C.., 1994. Isotope and chemical microsampling: Constraints on the history of an S-type rhyolite, San Vincenzo, Tuscany, Italy. Geochim. Cosmochim. Acta 58, 943–958. https://doi.org/10.1016/0016-7037(94)90517-7
Font, L., Davidson, J.P., Pearson, D.G., Nowell, G.M., Jerram, D.A., Ottley, C.J., 2008. Sr and Pb Isotope Micro-analysis of Plagioclase Crystals from Skye Lavas: an Insight into Open-system Processes in a Flood Basalt Province. J. Petrol. 49, 1449–1471. https://doi.org/10.1093/petrology/egn032
Gamble, J.A., Smith, I.E.M., McCulloch, M.T., Graham, I.J., Kokelaar, B.P., 1993. The geochemistry and petrogenesis of basalts from the Taupo Volcanic Zone and Kermadec Island Arc, SW Pacific. J. Volcanol. Geotherm. Res. 54, 265–290.
Gao, J.-F., Zhou, M.-F., Robinson, P.T., Wang, C.Y., Zhao, J.-H., Malpas, J., 2015. Magma mixing recorded by Sr isotopes of plagioclase from dacites of the Quaternary Tengchong volcanic field, SE Tibetan Plateau. J. Asian Earth Sci. 98, 1–17. https://doi.org/10.1016/j.jseaes.2014.10.036
Giletti, B.J., Casserly, J.E.D., 1994. Strontium diffusion kinetics in plagioclase feldspars. Geochim. Cosmochim. Acta 58, 3785–3793.
Ginibre, C., Davidson, J.P., 2014. Sr Isotope Zoning in Plagioclase from Parinacota Volcano (Northern Chile): Quantifying Magma Mixing and Crustal Contamination. J. Petrol. 55, 1203–1238. https://doi.org/10.1093/petrology/egu023
Ginibre, C., Wörner, G., Kronz, A., 2007. Crystal zoning as an archive for magma evolution. Elements 3, 261–266. https://doi.org/10.2113/gselements.3.4.261
Graham, I.J., Cole, J.W., 1991. Petrogenesis of andesites and dacites of White Island volcano, Bay of Plenty, New Zealand, in light of new geochemical and isotopic data. N. Z. J. Geol. Geophys. 34, 279–294.
Halama, R., Waight, T., Markl, G., 2002. Geochemical and isotopic zoning patterns of plagioclase megacrysts in gabbroic dykes from the Gardar Province, South Greenland: implications for crystallisation processes in anorthositic magmas. Contrib. Mineral. Petrol. 144, 109–127. https://doi.org/10.1007/s00410-002-0388-z
Hildreth, W., 2004. Volcanological perspectives on Long Valley, Mammoth Mountain, and Mono Craters: several contiguous but discrete systems. J. Volcanol. Geotherm. Res. 136, 169–198.
Houghton, B.F., Wilson, C.J.N., McWilliams, M.O., Lanphere, M.A., Weaver, S.D., Briggs, R.M., Pringle, M.S., 1995. Chronology and dynamics of a large silicic magmatic system: central Taupo Volcanic Zone, New Zealand. Geology 23, 13–16. https://doi.org/10.1130/0091-7613(1995)023<0013:CADOAL>2.3.CO;2
Humphreys, M.C.S., Blundy, J.D., Sparks, R.S.J., 2006. Magma Evolution and Open-System Processes at Shiveluch Volcano: Insights from Phenocryst Zoning. J. Petrol. 47, 2303–2334. https://doi.org/10.1093/petrology/egl045
Kawasaki, N., Itoh, S., Sakamoto, N., Yurimoto, H., 2017. Chronological study of oxygen isotope composition for the solar protoplanetary disk recorded in a fluffy Type A CAI from Vigarano. Geochim. Cosmochim. Acta 201, 83–102. https://doi.org/10.1016/j.gca.2015.12.031
Kawasaki, N., Kato, C., Itoh, S., Wakaki, S., Ito, M., Yurimoto, H., 2015. 26Al–26Mg chronology and oxygen isotope distributions of multiple melting for a Type C CAI from Allende. Geochim. Cosmochim. Acta 169, 99–114. https://doi.org/10.1016/j.gca.2015.07.037
Kennedy, A.K., Hutcheon, I.D., Wyllie, P.J., Wasserburg, G.J., 1990. Ion microprobe analysis of 87Sr/86 Sr in carbonates, in: Seventh International Conference on Geochronology, Cosmochronology and Isotope Geology.

Kimura, J.-I., Takahashi, T., Chang, Q., 2013. A new analytical bias correction for in situ Sr isotope analysis of plagioclase crystals using laser-ablation multiple-collector inductively coupled plasma mass spectrometry. J. Anal. At. Spectrom. 28, 945. https://doi.org/10.1039/c3ja30329b

Klemetti, E.W., Deering, C.D., Cooper, K.M., Roeske, S.M., 2011. Magmatic perturbations in the Okataina Volcanic Complex, New Zealand at thousand-year timescales recorded in single zircon crystals. Earth Planet. Sci. Lett. 305, 185–194.

Lange, A.E., Nielsen, R.L., Tepley, F.J., Kent, A.J.R., 2013. Diverse Sr isotope signatures preserved in mid-oceanic-ridge basalt plagioclase. Geology 41, 279–282. https://doi.org/10.1130/G33739.1

Leonard, G.S., Cole, J.W., Nairn, I.A., Self, S., 2002. Basalt triggering of the c. AD 1305 Kaharoa rhyolite eruption, Tarawera volcanic complex, New Zealand. J. Volcanol. Geotherm. Res. 115, 461–486. https://doi.org/10.1016/S0377-0273(01)00326-2

Ludwig, K.R., 2003. User's manual for isoplot 3.00, a geochronlogical toolkit for microsoft excel, in: Berkeley Geochronology Center Special Publication. p. 74.

McCulloch, M.T., Kyser, T.K., Woodhead, J.D., Kinsley, L., 1994. Pb-Sr-Nd-O isotopic constraints on the origin of rhyolites from the Taupo Volcanic Zone of New Zealand: evidence for assimilation followed by fractionation from basalt. Contrib. Mineral. Petrol. 115, 303–312.

Miller, J.A., Kent, A.J.R., 2009. The determination of maternal run time in juvenile Chinook salmon (Oncorhynchus tshawytscha) based on Sr/Ca and 87Sr/86Sr within otolith cores. Fish. Res. 95, 373–378. https://doi.org/10.1016/j.fishres.2008.09.030

Morgan, D.J., Jerram, D.A., Chertkoff, D.G., Davidson, J.P., Pearson, D.G., Kronz, A., Nowell, G.M., 2007. Combining CSD and isotopic microanalysis: Magma supply and mixing processes at Stromboli Volcano, Aeolian Islands, Italy. Earth Planet. Sci. Lett. 260, 419–431. https://doi.org/10.1016/j.epsl.2007.05.037

Nairn, I.., Shane, P.., Cole, J.., Leonard, G.., Self, S., Pearson, N., 2004. Rhyolite magma processes of the ~AD 1315 Kaharoa eruption episode, Tarawera volcano, New Zealand. J. Volcanol. Geotherm. Res. 131, 265–294. https://doi.org/10.1016/S0377-0273(03)00381-0

Nairn, I.A., 2002. Geology of the Okataina Volcanic Centre. GNS Geologic Map 25.

Nairn, I.A., Hedenquist, J.W., Villamor, P., Berryman, K.R., Shane, P.A.R., 2005. The ~AD1315 Tarawera and Waiotapu eruptions, New Zealand: contemporaneous rhyolite and hydrothermal eruptions driven by an arrested basalt dike system? Bull. Volcanol. 67, 186–193. https://doi.org/10.1007/s00445-004-0373-7

Nairn, I.A., Self, S., Cole, J.W., Leonard, G.S., Scutter, C., 2001. Distribution, stratigraphy, and history of proximal deposits from the c. AD 1305 Kaharoa eruptive episode at Tarawera Volcano, New Zealand. N. Z. J. Geol. Geophys. 44, 467–484. https://doi.org/10.1080/00288306.2001.9514950

Price, R., Mortimer, N., Smith, I., Maas, R., 2015. Whole-rock geochemical reference data for Torlesse and Waipapa terranes, North Island, New Zealand. N. Z. J. Geol. Geophys. 58, 213–228. https://doi.org/10.1080/00288306.2015.1026832

Ramos, F.C., Reid, M.R., 2005. Distinguishing Melting of Heterogeneous Mantle Sources from Crustal Contamination: Insights from Sr Isotopes at the Phenocryst Scale, Pisgah Crater, California. J. Petrol. 46, 999–1012. https://doi.org/10.1093/petrology/egi008

Ramos, F.C., Tepley III, F.J., 2008. Inter- and Intracrystalline Isotopic Disequilibria: Techniques and Applications. Rev. Mineral. Geochem. 69, 403–443. https://doi.org/10.2138/rmg.2008.69.11

Ramos, F.C., Wolff, J.A., Tollstrup, D.L., 2005. Sr isotope disequilibrium in Columbia River flood basalts: Evidence for rapid shallow-level open-system processes. Geology 33, 457. https://doi.org/10.1130/G21512.1

Ramos, F.C., Wolff, J.A., Tollstrup, D.L., 2004. Measuring 87Sr/86Sr variations in minerals and groundmass from basalts using LA-MC-ICPMS. Chem. Geol. 211, 135–158. https://doi.org/10.1016/j.chemgeo.2004.06.025

Rosman, K.J.R., Taylor, P.D.P., 1998. Isotopic compositions of the elements 1997 (Technical Report). Pure Appl. Chem. 70, 217–235. https://doi.org/10.1351/pac199870010217

Sahetapy-Engel, S., Self, S., Carey, R.J., Nairn, I.A., 2014. Deposition and generation of multiple widespread fall units from the c. AD 1314 Kaharoa rhyolitic eruption, Tarawera, New Zealand. Bull. Volcanol. 76. https://doi.org/10.1007/s00445-014-0836-4

Salisbury, M.J., Bohrson, W.A., Clynne, M.A., Ramos, F.C., Hoskin, P., 2008. Multiple Plagioclase Crystal Populations Identified by Crystal Size Distribution and in situ Chemical Data: Implications for

Timescales of Magma Chamber Processes Associated with the 1915 Eruption of Lassen Peak, CA. J. Petrol. 49, 1755–1780. https://doi.org/10.1093/petrology/egn045

Sano, Y., Shirai, K., Takahata, N., Amakawa, H., Otake, T., 2008. Ion microprobe Sr isotope analysis of carbonates with about 5μm spatial resolution: An example from an ayu otolith. Appl. Geochem. 23, 2406–2413. https://doi.org/10.1016/j.apgeochem.2008.02.027

Scatena-Wachel, D.E., 1986. Ion microprobe measurements of radiogenic nuclides: Cosmochemical and geochemical tracers. University of Chicago, Department of Chemistry.

Shane, P.A.R., 2015. Contrasting plagioclase textures and geochemistry in response to magma dynamics in an intra-caldera rhyolite system, Okataina volcano. J. Volcanol. Geotherm. Res. 297, 1–10. https://doi.org/10.1016/j.jvolgeores.2015.03.013

Shane, P.A.R., Martin, S.B., Smith, V.C., Beggs, K.F., Darragh, M.B., Cole, J.W., Nairn, I.A., 2007. Multiple rhyolite magmas and basalt injection in the 17.7 ka Rerewhakaaitu eruption episode from Tarawera volcanic complex, New Zealand. J. Volcanol. Geotherm. Res. 164, 1–26. https://doi.org/10.1016/j.jvolgeores.2007.04.003

Shane, P.A.R., Nairn, I.A., Smith, V.C., Darragh, M., Beggs, K., Cole, J.W., 2008. Silicic recharge of multiple rhyolite magmas by basaltic intrusion during the 22.6 ka Okareka Eruption Episode, New Zealand. Lithos 103, 527–549. https://doi.org/10.1016/j.lithos.2007.11.002

Singer, B.S., Dungan, M.A., Layne, G.D., 1995. Textures and Sr, Ba, Mg, Fe, K, and Ti compositional profiles in volcanic plagioclase: clues to the dynamics of calc-alkaline magma chambers. Am. Mineral. 80, 776–798.

Smith, V.C., Shane, P.A.R., Nairn, I.A., 2010. Insights into silicic melt generation using plagioclase, quartz and melt inclusions from the caldera-forming Rotoiti eruption, Taupo volcanic zone, New Zealand. Contrib. Mineral. Petrol. 160, 951–971. https://doi.org/10.1007/s00410-010-0516-0

Smith, V.C., Shane, P.A.R., Nairn, I.A., 2005. Trends in rhyolite geochemistry, mineralogy, and magma storage during the last 50 kyr at Okataina and Taupo volcanic centres, Taupo Volcanic Zone, New Zealand. J. Volcanol. Geotherm. Res. 148, 372–406. https://doi.org/10.1016/j.jvolgeores.2005.05.005

Smith, V.C., Shane, P.A.R., Nairn, I.A., 2004. Reactivation of a rhyolitic magma body by new rhyolitic intrusion before the 15.8 ka Rotorua eruptive episode: implications for magma storage in the Okataina Volcanic Centre, New Zealand. J. Geol. Soc. 161, 757–772.

Smith, V.C., Shane, P.A.R., Nairn, I.A., Williams, C.M., 2006. Geochemistry and magmatic properties of eruption episodes from Haroharo linear vent zone, Okataina Volcanic Centre, New Zealand during the last 10 kyr. Bull. Volcanol. 69, 57–88. https://doi.org/10.1007/s00445-006-0056-7

Stern, T.A., 1987. Asymmetric back-arc spreading, heat flux and structure associated with the Central Volcanic Region of New Zealand. Earth Planet. Sci. Lett. 85, 265–276.

Storm, S., Schmitt, A.K., Shane, P.A.R., Lindsay, J.M., 2014. Zircon trace element chemistry at sub-micrometer resolution for Tarawera volcano, New Zealand, and implications for rhyolite magma evolution. Contrib. Mineral. Petrol. 167, 1000. https://doi.org/10.1007/s00410-014-1000-z

Storm, S., Shane, P.A.R., Schmitt, A.K., Lindsay, J.M., 2012. Decoupled crystallization and eruption histories of the rhyolite magmatic system at Tarawera volcano revealed by zircon ages and growth rates. Contrib. Mineral. Petrol. 163, 505–519. https://doi.org/10.1007/s00410-011-0682-8

Storm, S., Shane, P.A.R., Schmitt, A.K., Lindsay, J.M., 2011. Contrasting punctuated zircon growth in two syn-erupted rhyolite magmas from Tarawera volcano: Insights to crystal diversity in magmatic systems. Earth Planet. Sci. Lett. 301, 511–520. https://doi.org/10.1016/j.epsl.2010.11.034

Streck, M.J., 2008. Time Scales of Magmatic Processes from Modeling the Zoning Patterns of Crystals. Rev. Mineral. Geochem. 69, 595–622. https://doi.org/10.2138/rmg.2008.69.14

Takahashi, T., Hirahara, Y., Miyazaki, T., Senda, R., Chang, Q., Kimura, J.I., Tatsumi, Y., 2013. Primary Magmas at the Volcanic Front of the NE Japan Arc: Coeval Eruption of Crustal Low-K Tholeiitic and Mantle-derived Medium-K Calc-Alkaline Basalts at Azuma Volcano. J. Petrol. 54, 103–148. https://doi.org/10.1093/petrology/egs065

Takahashi, T., Yoshikawa, M., Shibata, T., Tatsumi, Y., Shimizu, N., 2006. Sr isotopic micro analyses of plagioclase in andesites from Zao Volcano, NE Japan. Front. Res. Earth Evol. 2, 1–5.

Tepley III, F.J., Davidson, J.P., 2003. Mineral-scale Sr-isotope constraints on magma evolution and chamber dynamics in the Rum layered intrusion, Scotland. Contrib. Mineral. Petrol. 145, 628–641. https://doi.org/10.1007/s00410-003-0481-y

Tepley III, F.J., Davidson, J.P., Clynne, M.A., 1999. Magmatic interactions as recorded in plagioclase phenocrysts of Chaos Crags, Lassen Volcanic Center, California. J. Petrol. 40, 787–806.

Tepley III, F.J., Davidson, J.P., Tilling, R.I., Arth, J.G., 2000. Magma mixing, recharge and eruption histories recorded in plagioclase phenocrysts from El Chichon Volcano, Mexico. J. Petrol. 41, 1397–1411.

Ustunisik, G., Kilinc, A., Nielsen, R.L., 2014. New insights into the processes controlling compositional zoning in plagioclase. Lithos 200–201, 80–93. https://doi.org/10.1016/j.lithos.2014.03.021

Valley, J.W., Kita, N.T., 2009. In situ oxygen isotope geochemistry by ion microprobe. MAC Short Course Second. Ion Mass Spectrom. Earth Sci. 41, 19–63.

Vroon, P.Z., van der Wagt, B., Koornneef, J.M., Davies, G.R., 2008. Problems in obtaining precise and accurate Sr isotope analysis from geological materials using laser ablation MC-ICPMS. Anal. Bioanal. Chem. 390, 465–476. https://doi.org/10.1007/s00216-007-1742-9

Waight, T., Baker, J., Peate, D., 2002. Sr isotope ratio measurements by double-focusing MC-ICPMS: techniques, observations and pitfalls. Int. J. Mass Spectrom. 221, 229–244.

Waight, T. E., Dean, A.A., Maas, R., Nicholls, I.A., 2000. Sr and Nd isotopic investigations towards the origin of feldspar megacrysts in microgranular enclaves in two I- type plutons of the Lachlan Fold Belt, southeast Australia. Aust. J. Earth Sci. 47, 1105–1112. https://doi.org/10.1046/j.1440-0952.2000.00831.x

Waight, Tod E., Maas, R., Nicholls, I.A., 2000. Fingerprinting feldspar phenocrysts using crystal isotopic composition stratigraphy: implications for crystal transfer and magma mingling in S-type granites. Contrib. Mineral. Petrol. 139, 227–239. https://doi.org/10.1007/s004100000128

Wallace, L.M., Reyners, M., Cochran, U., Bannister, S., Barnes, P.M., Berryman, K., Downes, G., Eberhart-Phillips, D., Fagereng, A., Ellis, S., Nicol, A., McCaffrey, R., Beavan, R.J., Henrys, S., Sutherland, R., Barker, D.H.N., Litchfield, N., Townend, J., Robinson, R., Bell, R., Wilson, K., Power, W., 2009. Characterizing the seismogenic zone of a major plate boundary subduction thrust: Hikurangi Margin, New Zealand. Geochem. Geophys. Geosystems 10, n/a-n/a. https://doi.org/10.1029/2009GC002610

Weber, P.K., Bacon, C.R., Hutcheon, I.D., Ingram, B.L., Wooden, J.L., 2005. Ion microprobe measurement of strontium isotopes in calcium carbonate with application to salmon otoliths. Geochim. Cosmochim. Acta 69, 1225–1239. https://doi.org/10.1016/j.gca.2004.05.051

Wilson, C.J.N., Charlier, B.L.A., 2016. The life and times of silicic volcanic systems. Elements 12, 103–108. https://doi.org/10.2113/gselements.12.2.103

Wilson, C.J.N., Rogan, A.M., Smith, I.E.M., Northey, D.J., Nairn, I.A., Houghton, B.F., 1984. Caldera volcanoes of the Taupo volcanic zone, New Zealand. J. Geophys. Res. Solid Earth 89, 8463–8484.

Wilson, C.J.N., Rowland, J.V., 2016. The volcanic, magmatic and tectonic setting of the Taupo Volcanic Zone, New Zealand, reviewed from a geothermal perspective. Geothermics 59, 168–187. https://doi.org/10.1016/j.geothermics.2015.06.013

Wolff, J.A., Ramos, F.C., Davidson, J.P., 1999. Sr isotope disequilibrium during differentiation of the Bandelier Tuff: constraints on the crystallization of a large rhyolitic magma chamber. Geology 27, 495–498.

Yang, S.-H., Maier, W.D., Lahaye, Y., O'Brien, H., 2013. Strontium isotope disequilibrium of plagioclase in the Upper Critical Zone of the Bushveld Complex: evidence for mixing of crystal slurries. Contrib. Mineral. Petrol. 166, 959–974. https://doi.org/10.1007/s00410-013-0903-4

Zellmer, G.F., Blake, S., Vance, D., Hawkesworth, C., Turner, S., 1999. Plagioclase residence times at two island arc volcanoes (Kameni Islands, Santorini, and Soufriere, St. Vincent) determined by Sr diffusion systematics. Contrib. Mineral. Petrol. 136, 345–357.

Figures and captions

Fig. 1. Map of the Okataina Volcanic Centre (OVC) showing caldera boundaries and intra-caldera volcanic centres (modelled after Smith et al., 2006). OVC is one of two currently active silicic centres within the Taupo Volcanic Zone (TVZ; shaded region in upper left image). North Island Fault System (NIFS) shown on inset map is from Wilson and Rowland (2016). Subduction rates shown on the inset map are from Wallace et al. (2009).

Fig. 2. (A) An annotated BSE image of a Kaharoa plagioclase crystal showing the locations of MC-SIMS analytical sites (yellow spots), the LA-MC-ICP-MS trough (white oval with arrow indicating direction of analysis), and EMPA analytical sites with their respective An contents (blue spots and text). The straight white lines and adjacent numbers list the specific $^{87}Sr/^{86}Sr$ ratio of the MC-SIMS analytical site they point to, and the numbers listed in parenthesis near each MC-SIMS $^{87}Sr/^{86}Sr$ ratio indicate the sequential order in which the sites are shown on the graph in part C. Distances from core-to-rim were measured along the LA-MC-ICP-MS trough. MC-SIMS sites that are not situated parallel to the LA-MC-ICP-MS trough were grouped with MC-SIMS site that are situated parallel to the trough and represent the same compositional domain (zone) within the crystal (for easier visibility, grouped MC-SIMS analyses have been plotted 5 μm apart on core-to-rim profiles). The core appears brighter relative to the rim due to higher An contents. (B) A reflected light image of the same crystal showing the relative size difference between LA-MC-ICP-MS analysis (85 μm) and ion microprobe sites (12 μm). (C) A graph illustrating the core-to-rim variability of $^{87}Sr/^{86}Sr$ ratios and An contents of the Kaharoa plagioclase crystal in part A. The yellow spots represent $^{87}Sr/^{86}Sr$ ratios of specific sites acquired via MC-SIMS, with their respective errors shown as vertical black lines. The dashed, horizontal black lines represent $^{87}Sr/^{86}Sr$ ratios acquired via LA-MC-ICP-MS for the plagioclase core and rim, and the grey envelope surrounding each dash line indicates the associated error. The bright blue line represents An contents calculated using EMPA data.

Fig. 3. BSE images of representative plagioclase crystals selected for analyses, with common zoning patterns and mineral textures. The yellow spots represent $^{87}Sr/^{86}Sr$ ratios of specific sites acquired via MC-SIMS, with their respective errors shown as vertical black lines. The dashed, horizontal black lines represent $^{87}Sr/^{86}Sr$

ratios acquired via LA-MC-ICP-MS for the plagioclase core and rim, and the grey envelope surrounding each dash line indicates the associated error. The bright blue line represents An contents calculated using EMPA data. (A) Kaharoa crystal with boxy-cellular texture in the core. (B) Kaharoa crystal with a distinct and frayed transition from a sodic core to a calcic rim. (C) Rotoma crystal exhibiting gradual decrease in An contents from core to rim, as well as a zone with inclusions between core and rim.

Fig. 4. Histogram depicting LA-MC-ICP-MS $^{87}Sr/^{86}Sr$ ratios in OVC plagioclase. Individual (per crystal) ratios and respective errors are included in Figs. 2 – 3 and 5 – 6, and are listed in Table 2.

Fig. 5. Graphs illustrating the core-to-rim variability of $^{87}Sr/^{86}Sr$ ratios and An contents of Kaharoa plagioclase. The yellow spots represent $^{87}Sr/^{86}Sr$ ratios of specific sites acquired via MC-SIMS, with their respective errors shown as vertical black lines. The dashed, horizontal black lines represent $^{87}Sr/^{86}Sr$ ratios acquired via LA-MC-ICP-MS for the plagioclase core and rim, and the grey envelope surrounding each dash line indicates the associated error. The bright blue line represents An contents calculated using EMPA data.

Fig. 6. Graphs illustrating the core-to-rim variability of $^{87}Sr/^{86}Sr$ ratios and An contents of Rotoma plagioclase. The yellow spots represent $^{87}Sr/^{86}Sr$ ratios of specific sites acquired via MC-SIMS, with their respective errors shown as vertical black lines. The dashed, horizontal black lines represent $^{87}Sr/^{86}Sr$ ratios acquired via LA-MC-ICP-MS for the plagioclase core and rim, and the grey envelope surrounding each dash line indicates the associated error. The bright blue line represents An contents calculated using EMPA data.

Fig. 7. Graphical representation of correlation (matrix effect) between IMF-corrected MC-SIMS $^{87}Sr^{+}/^{86}Sr^{+}$ ion intensity ratios ($^{87}Sr^{+}/^{86}Sr^{+}_{SIMS}$) and EMPA An contents in plagioclase from Kaharoa and Rotoma (Table B1). The typical error bars on the bottom right represent the 2σ reproducibility for MC-SIMS and 2σ analytical error for EMPA. The solid grey line represents linear regression of MC-SIMS data and has a slope of 4.06 (± 0.78) × 10^{-5} and a y-intercept of 0.70669 (± 0.00029). The dotted grey lines provide the 1σ error envelope. The linear regression was used to correct for the matrix effect (see Section 4.3).

Figure 1

Click here to download high resolution image

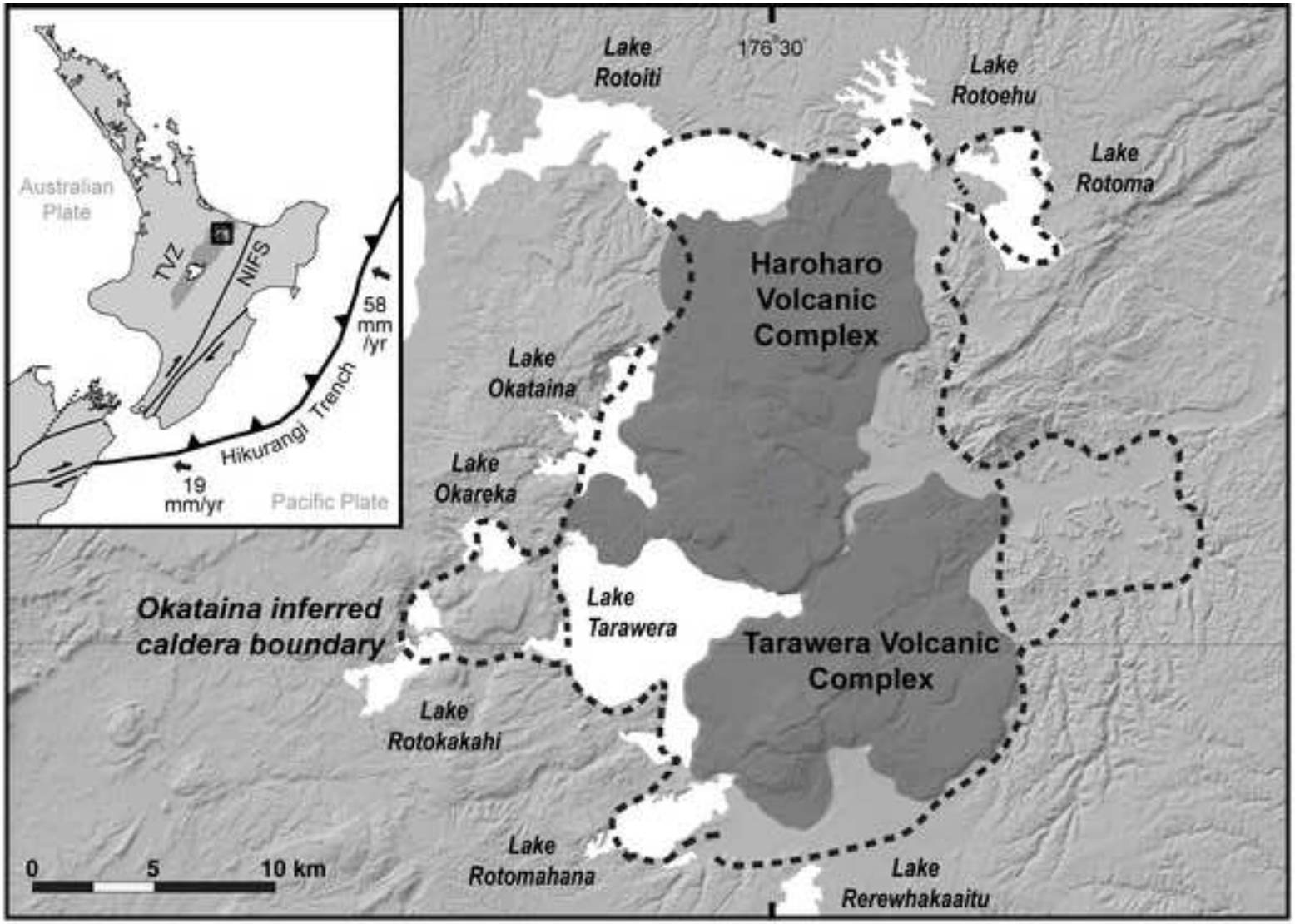

Figure 2

Click here to download high resolution image

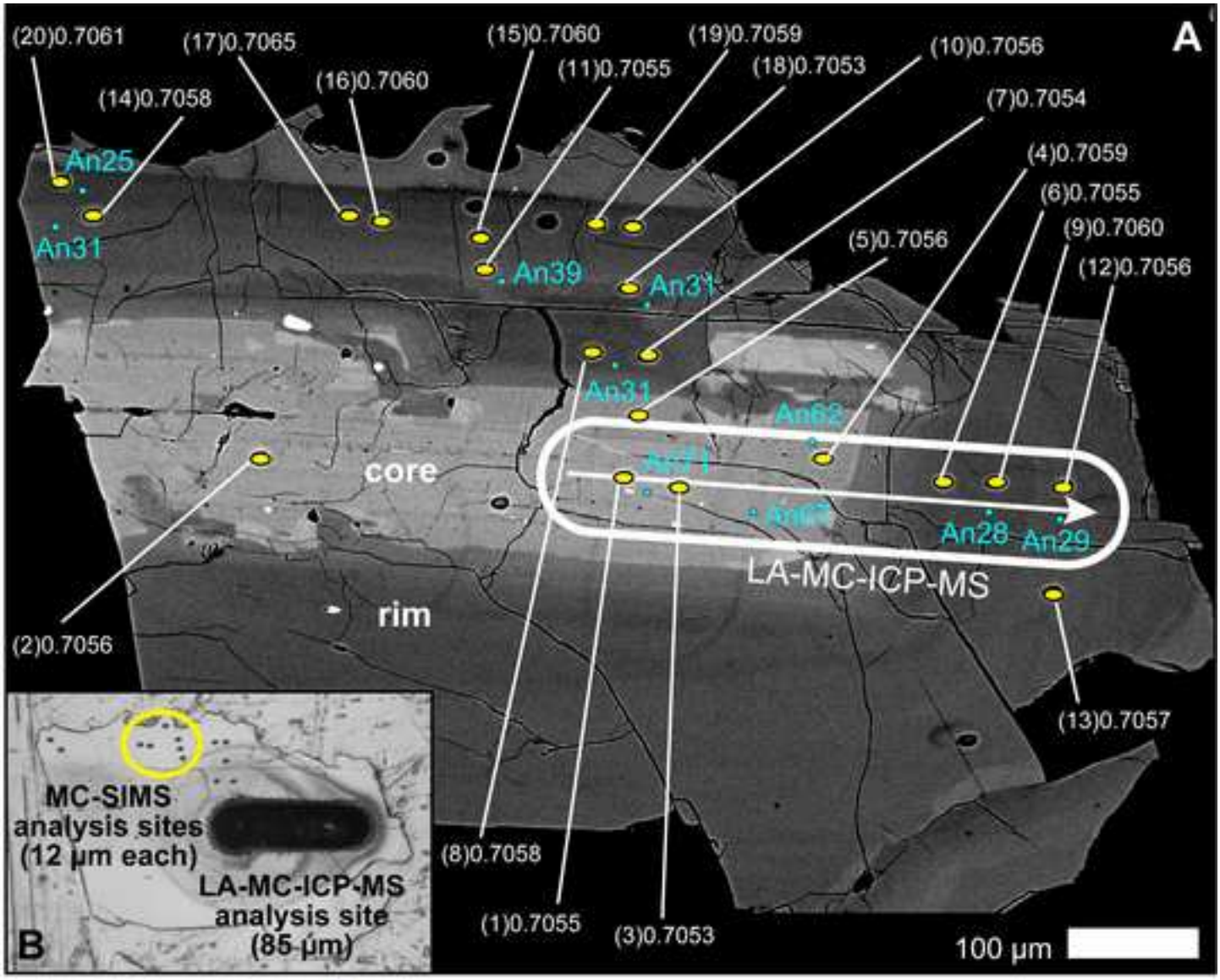

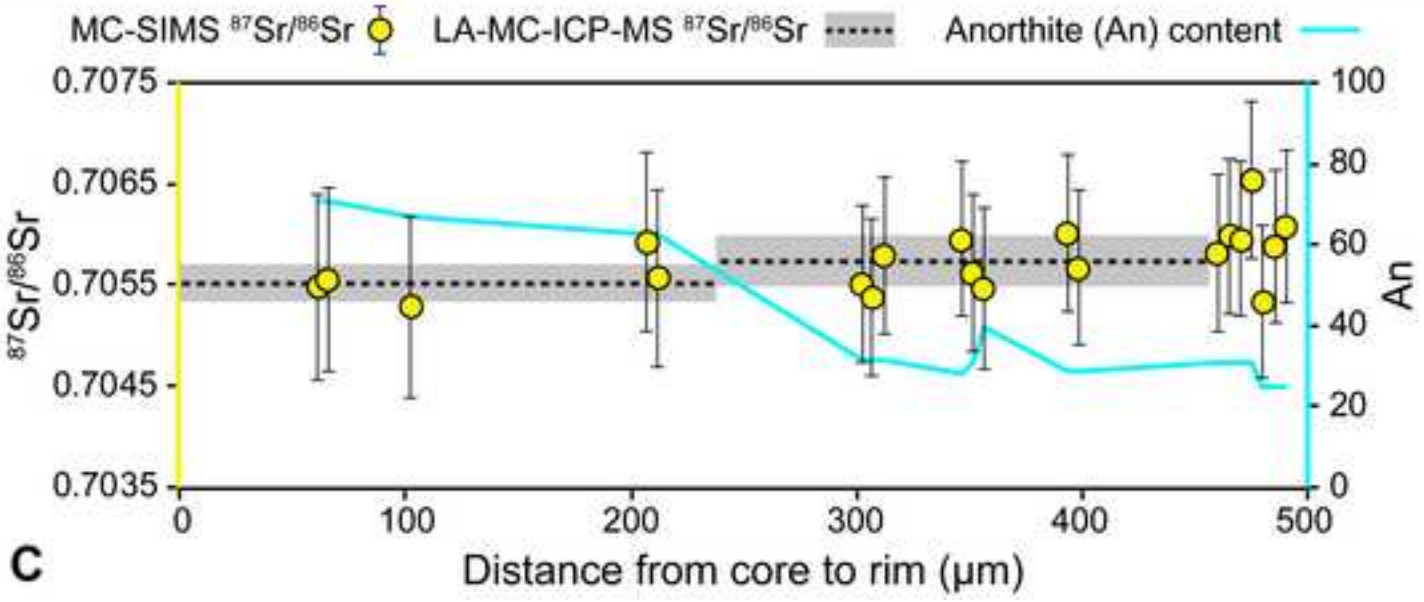

Figure 3

Click here to download high resolution image

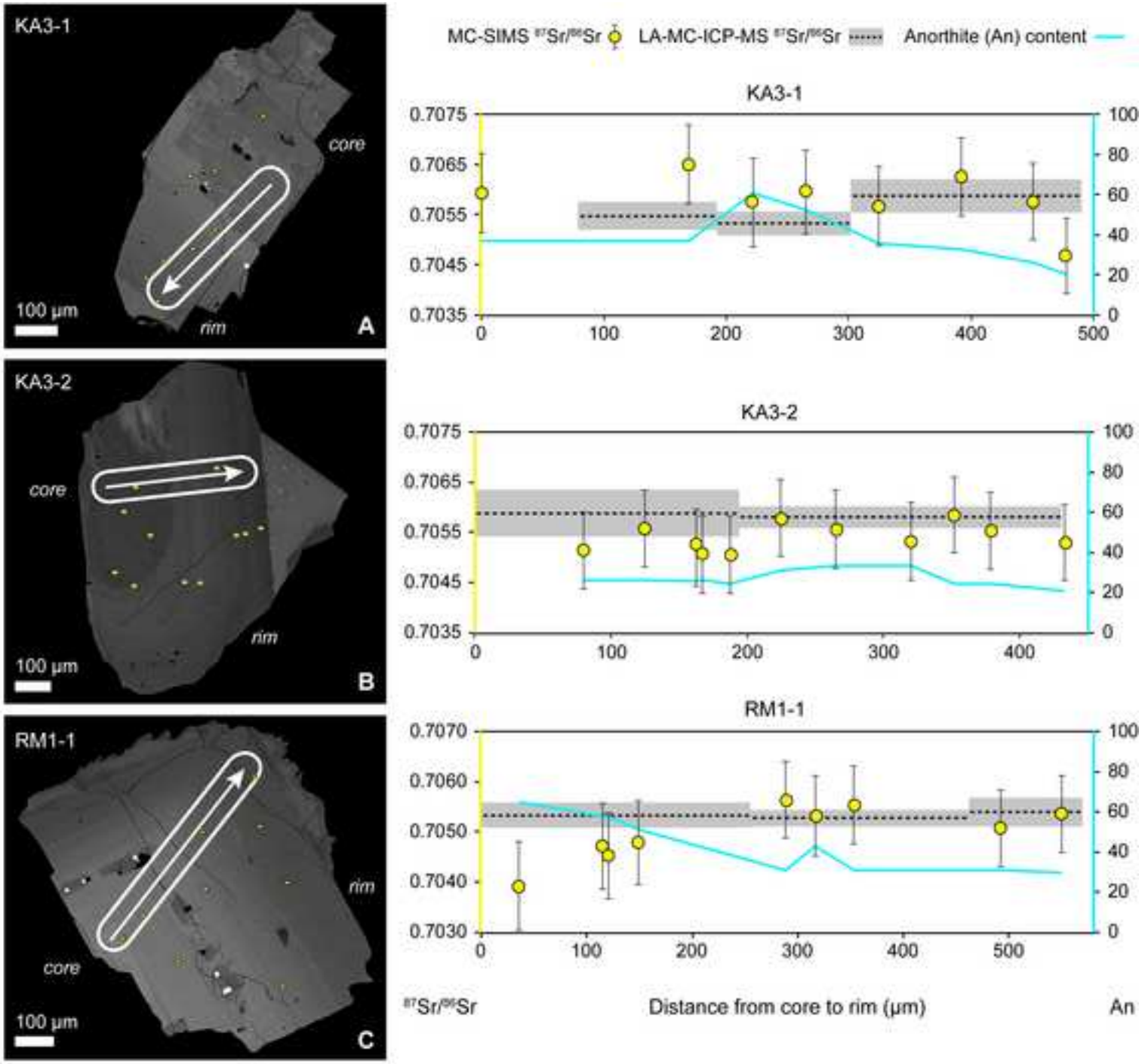

Figure 4
Click here to download high resolution image

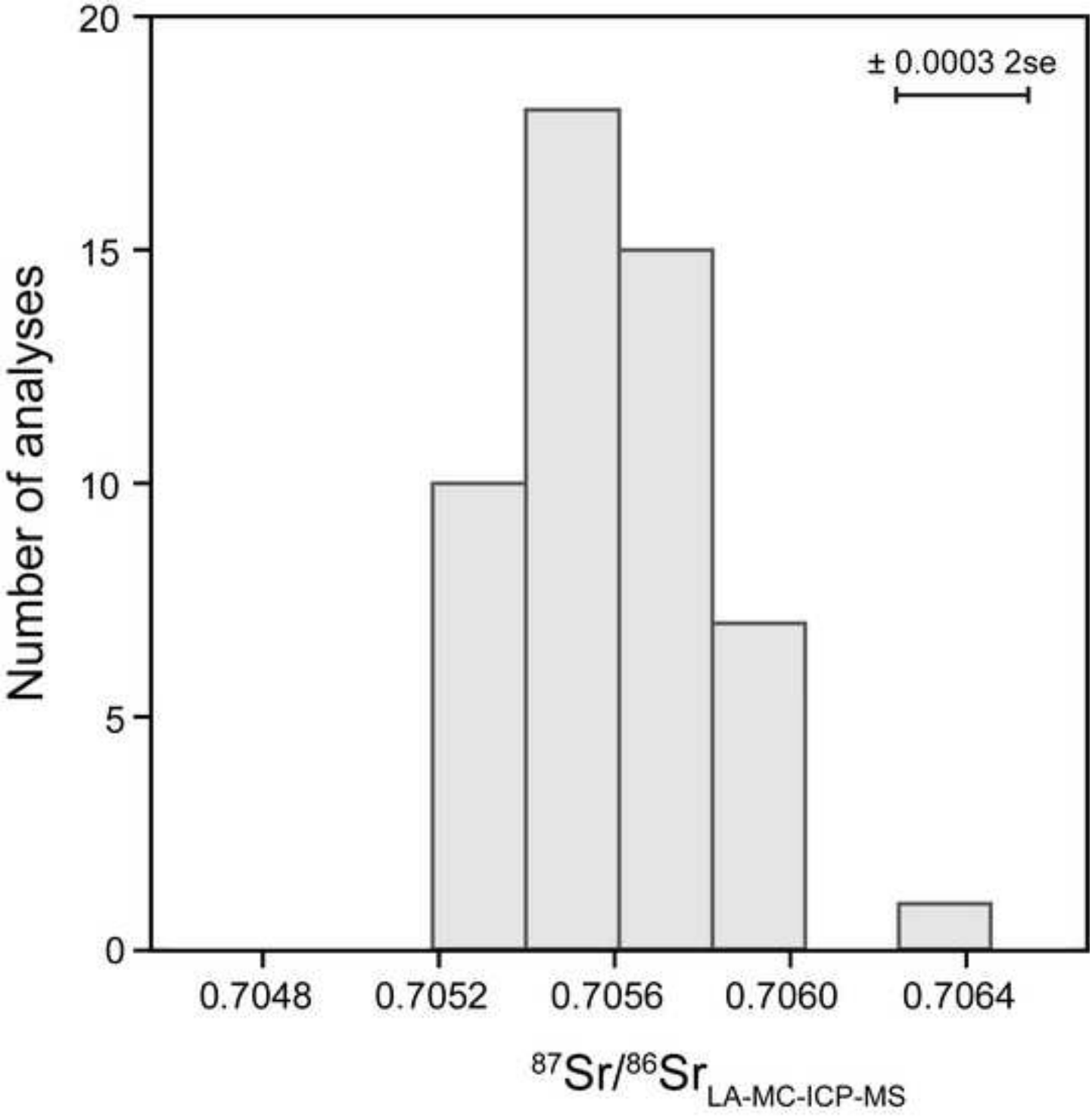

Figure 5

Click here to download high resolution image

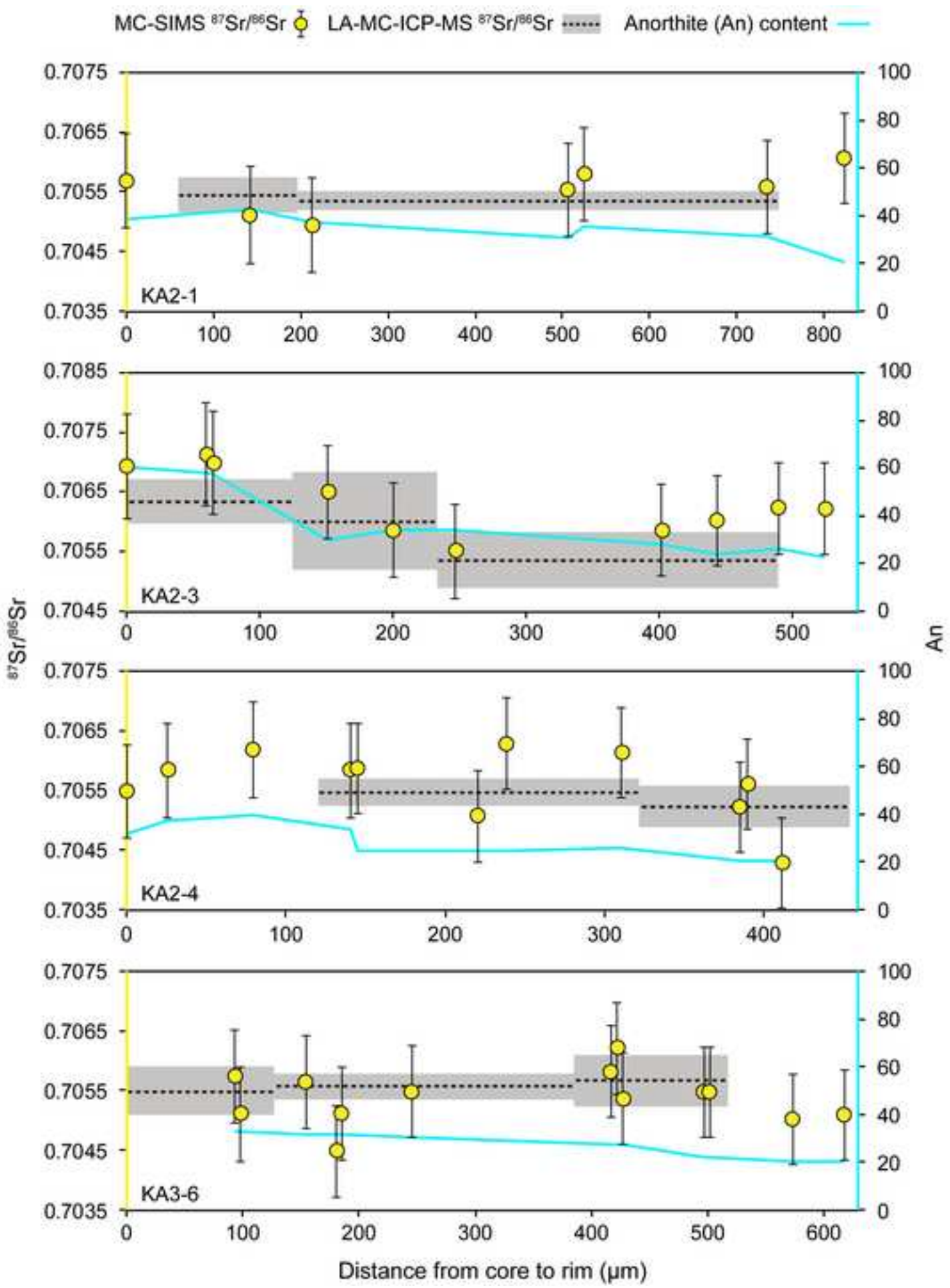

Figure 6

Click here to download high resolution image

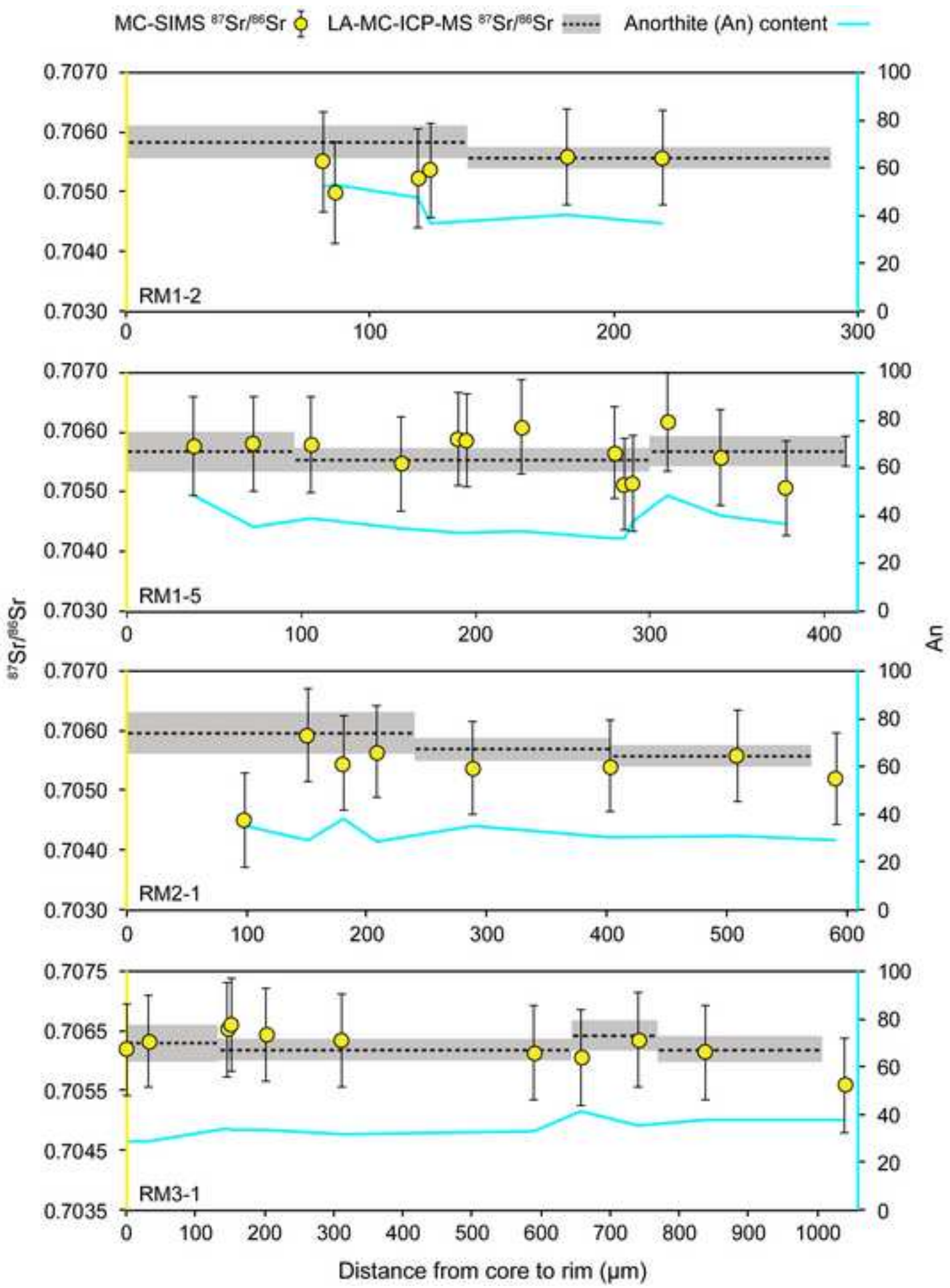

Figure 7

Click here to download high resolution image

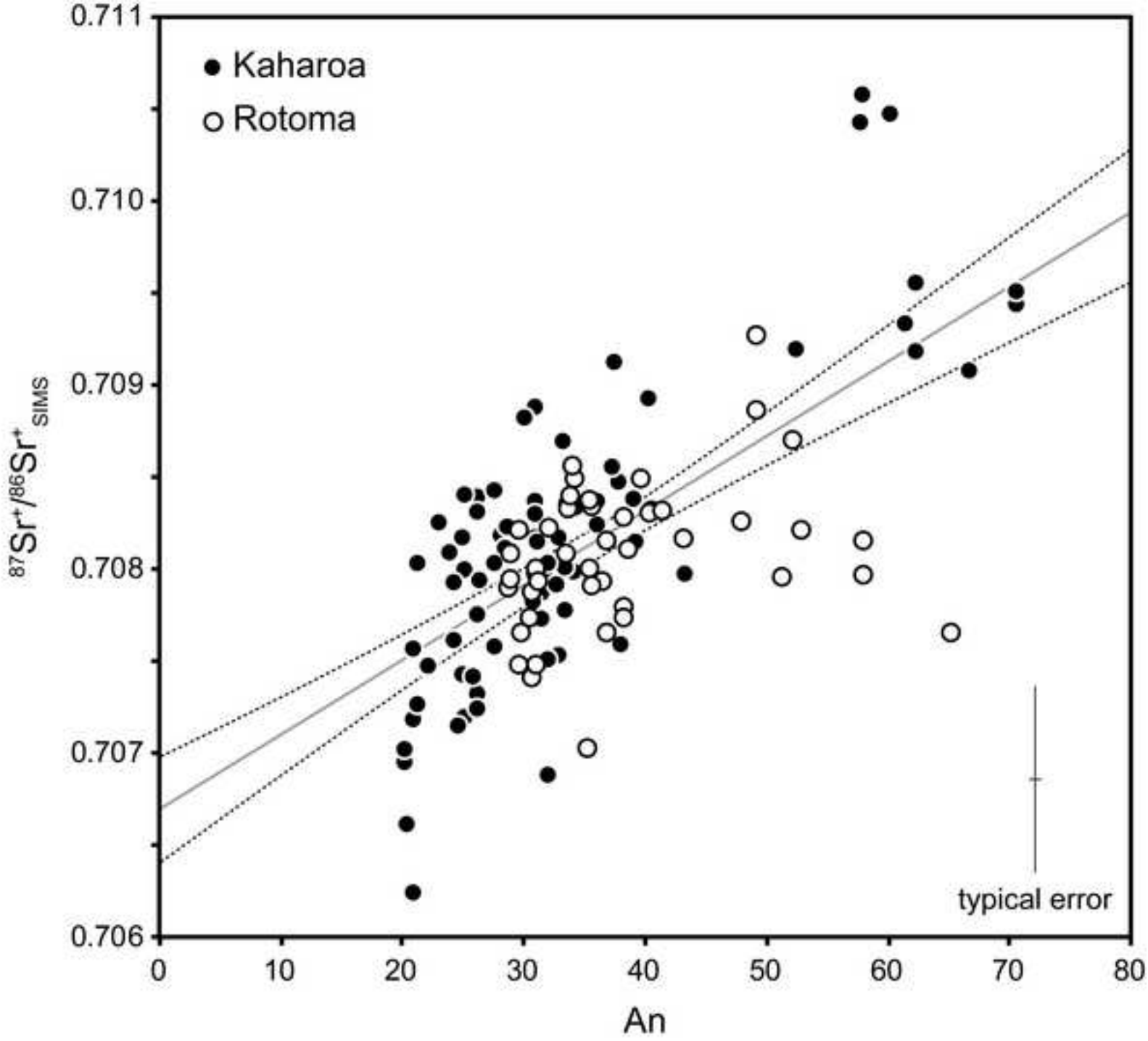

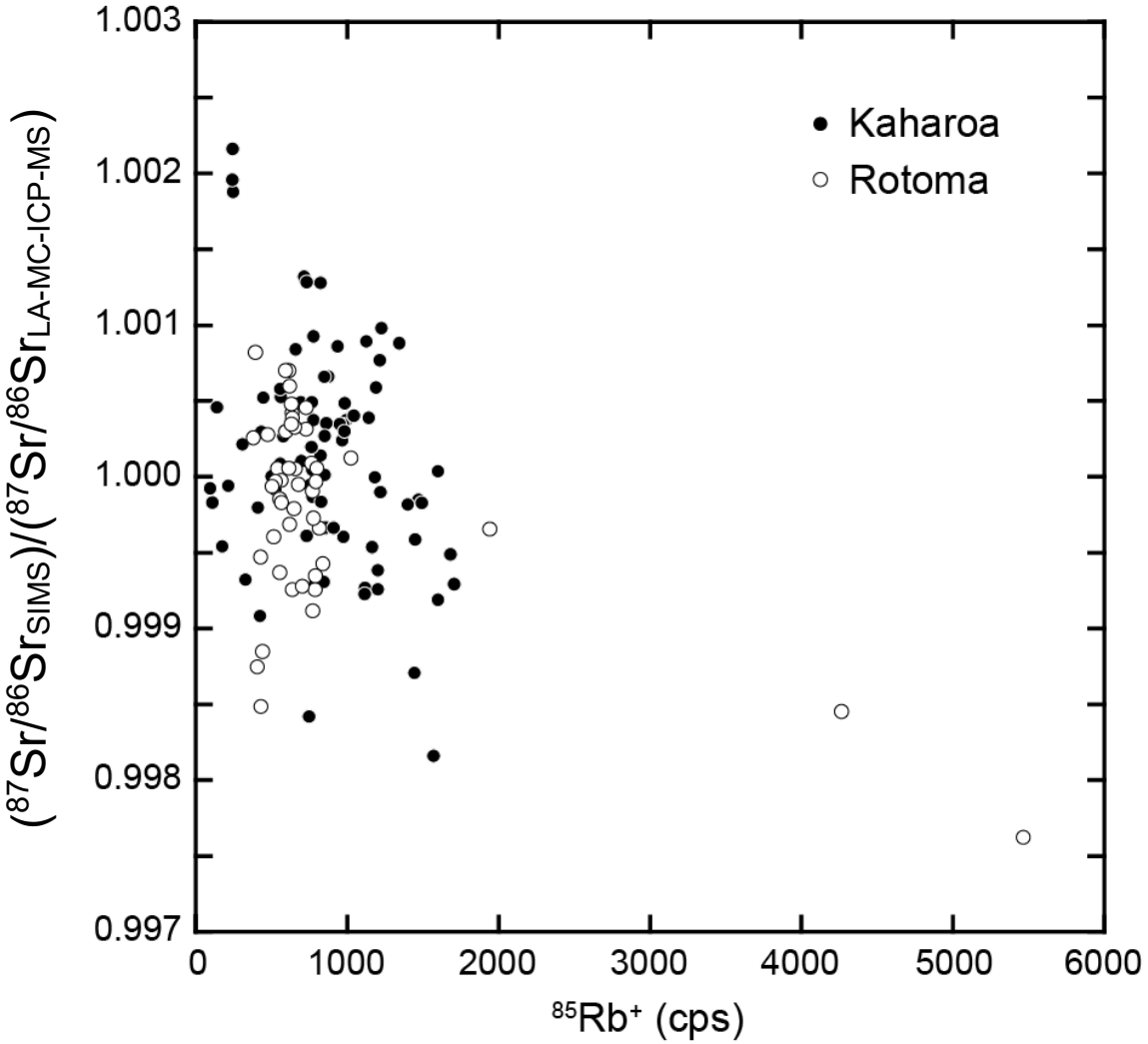

Fig. A1. Graphical representation of the relationship between secondary ion intensities of $^{85}Rb^{+}$ and $(^{87}Sr/^{86}Sr_{SIMS})/(^{87}Sr/^{86}Sr_{LA\text{-}MC\text{-}ICP\text{-}MS})$ ratios. Secondary ion intensities of $^{87}Rb^{+}$ calculated from those of $^{85}Rb^{+}$ (assuming a natural ratio $^{85}Rb/^{87}Rb = 2.5926$; Rosman and Taylor, 1998) are ca. 0.0101 (average) and 0.0520 (maximum) of secondary ion intensities of $^{87}Sr^{+} + ^{87}Rb^{+}$. Because instrumental mass fractionation between $^{86}Sr^{+}$ and $^{87}Sr^{+}$ for Miyakejima anorthite was ca. 0.0050 (average across four sessions of measurements), instrumental mass fractionation between $^{85}Rb^{+}$ and $^{87}Rb^{+}$ could be estimated to be ca. 0.0100 (0.0050 x 2, assuming both masses fractionate). Thus, effects of instrumental mass fractionation between $^{85}Rb^{+}$ and $^{87}Rb^{+}$ on corrected count rates of $^{87}Sr^{+}$ are always smaller than ca. 0.0005 (0.0100 x 0.0520), i.e., smaller than the given analytical errors.

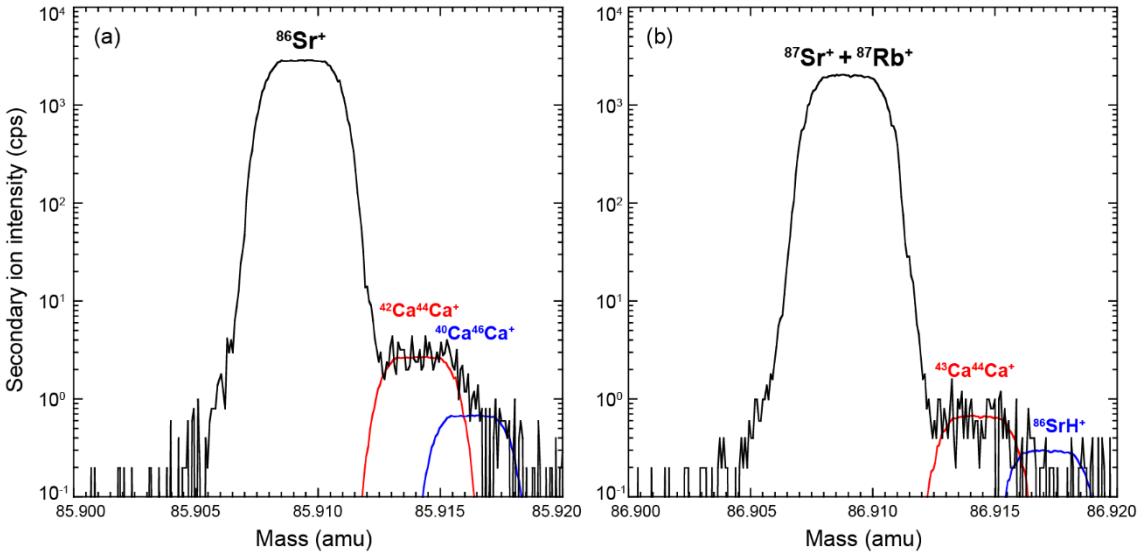

Fig. A2. High mass resolution spectra of secondary ions around (a) 85.91 atomic mass unit (amu) and (b) 86.91 amu, with mass resolution power (M/ΔM) of ~20,000, taken on Miyakejima anorthite. Mass resolution is defined as the mass of the peak divided by the base width of 10% peak level. As per natural abundances, contributions of $^{42}Ca^{44}Ca^+$ on $^{86}Sr^+$ are always larger than those of $^{43}Ca^{44}Ca^+$ on $^{87}Sr^+$. However, even for $^{42}Ca^{44}Ca^+$ on $^{86}Sr^+$, secondary ion intensities of $^{42}Ca^{44}Ca^+$ are ca. 0.00003 (average) and 0.00011 (maximum) of secondary ion intensities of $^{86}Sr^+ + {}^{42}Ca^{44}Ca^+$. In this study, secondary ion intensities of $^{42}Ca^{44}Ca^+$ (illustrated in this figure) were calculated from measured $^{40}Ca_2^+$ secondary ion intensities (Table B1) assuming $^{40}Ca/^{42}Ca$ = 149.8145 and $^{40}Ca/^{44}Ca$ = 46.3115 (Rosman and Taylor, 1998). By applying the same estimation we did for $^{87}Rb^+$ in Fig. A1, effects of instrumental mass fractionation and real variations in Ca-isotope ratios are clearly negligible for our measurements.

Supplementary Tables - Appendix B

Click here to download Table: B1-B2.pdf

Table B1. MC-SIMS analyses of OVC plagioclase

Spot No.	$^{40}Ca^{40}Ca^{+}$ (cts) 40*	$^{85}Rb^{+}$ (cts) 400*	Mass 86 (cts) 400*	Mass 87 (cts) 400*	$^{87}Sr^{+}/^{86}Sr^{+}_{raw}$	$^{87}Sr^{+}/^{86}Sr^{+}_{IMF}$	An
KA2-1@37	789236	331510	27461792	19580440	0.70837	0.70837	39
KA2-1@39	455502	133789	14656584	10427644	0.70797	0.70797	43
KA2-1@40	312823	172071	15213628	10831028	0.70758	0.70758	38
KA2-1@43	282268	213324	14985988	10690412	0.70788	0.70788	31
KA2-1@44	325525	175335	15248324	10868664	0.70836	0.70836	36
KA2-1@46	283273	202057	13720340	9791488	0.70798	0.70798	32
KA2-1@48	133141	351937	10055212	7254900	0.70802	0.70802	21
KA2-2@49	862897	46600	14786684	10507420	0.70943	0.70943	71
KA2-2@56	1177548	40173	14813616	10524816	0.70949	0.70949	71
K2-2@128	1264339	71615	20413756	14360240	0.70215	0.70907	67
KA2-2@50	834106	57781	14591252	10374728	0.70954	0.70954	62
K2-2@132	951414	87925	19995508	14075140	0.70225	0.70917	62
KA2-2@51	279072	222204	13556012	9681208	0.70786	0.70786	31
K2-2@129	360474	345917	20715976	14651320	0.70082	0.70772	31
KA2-2@57	286664	233449	14389212	10279544	0.70815	0.70815	31
K2-2@131	321654	395727	18864980	13381732	0.70126	0.70817	28
K2-2@133	268193	342484	21617064	15286472	0.70105	0.70795	31
KA2-2@81	360253	166522	14188476	10111328	0.70814	0.70814	39
KA2-2@52	253674	226730	12461060	8912456	0.70822	0.70822	29
KA2-2@59	274856	225448	12755700	9116632	0.70791	0.70791	29
KA2-2@84	351098	237133	14568684	10408124	0.70816	0.70816	31
KA2-2@83	247780	224900	13246172	9469524	0.70835	0.70835	31
KA2-2@86	234588	279686	13562436	9713844	0.70829	0.70829	31
KA2-2@53	211723	288606	12738476	9141128	0.70887	0.70887	31
KA2-2@88	178098	294626	11984892	8591880	0.70742	0.70742	25
K2-2@130	254594	459665	17137280	12191416	0.70106	0.70797	25
KA2-2@85	217853	342031	11925220	8576740	0.70816	0.70816	25
K2-3@135	757564	101008	22924216	16166140	0.70352	0.71046	60
K2-3@136	997612	98836	21231400	14976380	0.70363	0.71056	58
K2-3@137	1046180	98686	22478204	15850292	0.70348	0.71041	58
K2-3@138	372181	331339	19997916	14163960	0.70189	0.70881	30
K2-3@134	403794	313308	22552176	15939424	0.70143	0.70835	34
K2-3@139	433840	311358	21155032	14950972	0.70107	0.70798	34
K2-3@140	283523	400366	19693680	13963328	0.70119	0.70810	29
K2-3@141	230800	478779	18221388	12960748	0.70117	0.70808	24
K2-3@142	282815	452957	19400476	13783368	0.70147	0.70838	26
K2-3@143	234075	538850	17151536	12236620	0.70133	0.70824	23
K2-4@145	457554	590392	23611420	16778992	0.70100	0.70791	33
K2-4@146	577536	391282	24438648	17295468	0.70155	0.70846	38
K2-4@147	709875	265649	24360248	17202692	0.70199	0.70891	40
K2-4@148	469856	347004	20942748	14823056	0.70141	0.70833	34
K2-4@149	314815	418928	19917896	14125380	0.70108	0.70799	25
KA2-4@203	278488	448668	19115392	13552416	0.69994	0.70719	25
K2-4@144	283924	492452	20517452	14582400	0.70148	0.70840	25
K2-4@150	289666	487606	20136384	14311204	0.70138	0.70829	26
K2-4@151	176426	674644	16077120	11518476	0.70027	0.70717	21
K2-4@152	199418	641880	16717936	11960976	0.70066	0.70756	21
KA2-4@202	176470	630425	15149020	10832140	0.69900	0.70624	21
KA3-1@243	341821	308493	18816428	13314640	0.70130	0.70855	37
KA3-1@244	581651	294862	20045344	14182356	0.70186	0.70911	38
KA3-1@245	1117392	125234	20963180	14765564	0.70209	0.70932	61

KA3-1@246	905861	180054	22757616	16043344	0.70194	0.70918	53
KA3-1@247	509679	280849	21605024	15252688	0.70098	0.70823	36
KA3-1@248	409509	313020	19517244	13810536	0.70144	0.70869	33
KA3-1@249	283819	388924	16480312	11697284	0.70068	0.70793	27
KA3-1@250	182627	578950	11783112	8463944	0.69937	0.70660	21
KA3-2@214	252630	482764	15815164	11257852	0.70008	0.70732	26
KA3-2@205	263145	475461	17146852	12194624	0.70050	0.70775	26
KA3-2@206	261072	468085	16469268	11711608	0.70017	0.70741	26
KA3-2@213	218132	482728	16486852	11726596	0.69999	0.70723	26
KA3-2@207	277821	448008	17160620	12183336	0.69990	0.70714	25
KA3-2@208	362122	342856	18846608	13341436	0.70089	0.70814	31
KA3-2@209	404758	303974	19129980	13522476	0.70076	0.70800	33
K3-2@204	276830	391912	20295492	14368288	0.70052	0.70776	33
KA3-2@210	271478	382941	17729148	12569820	0.70067	0.70792	24
KA3-2@211	224010	489113	16873804	12006168	0.70036	0.70760	24
KA3-2@212	177685	581410	14817284	10596384	0.70001	0.70725	21
KA3-6@215	313149	307335	20171628	14256860	0.70091	0.70816	33
KA3-6@336	378532	317132	19353612	13699392	0.70154	0.70753	33
KA3-6@216	377595	310739	19106424	13508864	0.70077	0.70802	32
KA3-6@337	376240	301587	18226372	12890560	0.70088	0.70687	32
KA3-6@340	355921	339389	18285044	12957640	0.70150	0.70750	32
KA3-6@217	369426	333160	19443508	13749868	0.70057	0.70782	31
KA3-6@223	233129	394751	19960448	14139724	0.70077	0.70802	28
KA3-6@218	320718	377542	19207464	13612936	0.70116	0.70841	28
KA3-6@338	284044	365596	17683312	12546748	0.70156	0.70757	28
KA3-6@221	129111	562369	15956176	11389452	0.70021	0.70745	22
KA3-6@219	168136	598738	13046276	9366064	0.70022	0.70746	22
KA3-6@220	185952	642420	14961272	10716044	0.69970	0.70694	20
KA3-6@222	141586	684824	14760844	10593220	0.69977	0.70701	20
RM1-1@384	1218455	2188306	21916744	16222360	0.70171	0.70765	65
RM1-1@385	978560	164408	23561572	16607900	0.70221	0.70815	58
RM1-1@392	990225	174254	24393456	17191460	0.70203	0.70797	58
RM1-1@386	819504	178390	24745188	17439744	0.70202	0.70795	51
RM1-1@391	709587	218043	25623168	18072104	0.70204	0.70798	31
RM1-1@387	652590	208397	24938252	17591868	0.70221	0.70816	43
RM1-1@388	343367	309726	19043856	13485604	0.70187	0.70787	31
RM1-1@390	363079	317093	20129880	14241680	0.70143	0.70740	31
RM1-1@389	352070	328519	20009532	14166560	0.70167	0.70765	30
RM1-2@403	820674	223499	24417824	17245280	0.70275	0.70870	52
RM1-2@404	819573	311040	23962000	16946980	0.70226	0.70821	53
RM1-2@405	707034	173681	22948576	16183232	0.70230	0.70825	48
RM1-2@406	505458	778481	22376084	16007064	0.70196	0.70792	37
RM1-2@408	516482	227891	21025696	14854636	0.70234	0.70831	40
RM1-2@409	478808	273715	22011128	15561000	0.70218	0.70815	37
RM1-5@418	670381	154691	19218440	13567332	0.70287	0.70886	49
RM1-5@419	415428	239255	18896912	13364088	0.70234	0.70834	36
RM1-5@420	516240	191841	19151056	13527204	0.70250	0.70849	40
RM1-5@421	446452	229000	19312248	13645464	0.70201	0.70800	35
RM1-5@422	395999	255821	19929824	14096324	0.70236	0.70835	34
RM1-5@423	397180	256690	19651540	13900704	0.70234	0.70832	34
RM1-5@424	413384	247955	19183796	13573152	0.70256	0.70856	34
RM1-5@425	345107	307992	20463620	14484436	0.70202	0.70800	31
RM1-5@426	344232	317929	20593724	14568908	0.70150	0.70748	31
RM1-5@427	504371	223664	20863320	14728136	0.70182	0.70779	38
RM1-5@428	695669	159390	20793468	14684672	0.70328	0.70926	49

RM1-5@429	555384	212351	20728788	14639808	0.70232	0.70830	40
RM1-5@430	458288	256971	20285692	14332772	0.70168	0.70765	37
RM2-1@368	355887	1708292	21132584	15473728	0.70105	0.70702	35
RM2-1@369	405303	292630	21375512	15123112	0.70223	0.70820	30
RM2-1@370	476403	261242	21833980	15430748	0.70213	0.70810	39
RM2-1@371	313084	322095	20155568	14271372	0.70191	0.70789	29
RM2-1@372	456221	250753	21895456	15465664	0.70194	0.70790	36
RM2-1@373	339111	312128	21516860	15219836	0.70176	0.70773	31
RM2-1@374	356572	319008	20487612	14504040	0.70195	0.70793	31
RM2-1@375	327500	337838	20051360	14196044	0.70150	0.70748	30
RM3-1@346	269392	412026	21179284	15025828	0.70196	0.70794	29
RM3-1@347	318290	292578	20005900	14158540	0.70209	0.70807	29
RM3-1@348	438165	250315	21426672	15148808	0.70252	0.70849	34
RM3-1@349	435999	238259	21005744	14849852	0.70258	0.70856	34
RM3-1@350	409046	254001	20690976	14631368	0.70242	0.70840	34
RM3-1@351	368725	263842	20136364	14241872	0.70223	0.70821	32
RM3-1@352	398682	265016	21105888	14920396	0.70210	0.70808	33
RM3-1@353	573323	204101	21920220	15473984	0.70235	0.70831	41
RM3-1@354	426483	254043	21353604	15096284	0.70239	0.70837	35
RM3-1@355	478090	247956	21162024	14957452	0.70230	0.70828	38
RM3-1@356	364056	284178	19468336	13771084	0.70174	0.70773	38

*measurement time (in seconds)

raw: ratios corrected for $^{87}Rb^{+}$ and Ca dimer interferences

IMF: ratios corrected for instrumental mass fractionation

Table B2. EMPA analyses of OVC plagioclase

Unit/Spot No.	SiO_2	Al_2O_3	FeO	MgO	CaO	Na_2O	K_2O	Total	An	Ab	Or
Kaharoa											
KA2-2_01	50.5	31.3	0.40	0.000	14.2	3.2	0.09	99.8	71	29	0.5
KA2-2_001	51.2	30.9	0.32	0.000	13.6	3.7	0.10	99.8	67	33	0.6
KA2-2_002	52.4	30.1	0.29	0.011	12.6	4.1	0.13	99.7	62	37	0.8
KA2-2_02	61.4	24.4	0.20	0.019	5.8	7.9	0.48	100.2	28	69	2.7
KA2-2_03	61.2	24.4	0.18	0.003	5.9	7.9	0.45	100.0	29	69	2.6
KA2-2_04	60.3	24.8	0.20	0.007	6.5	7.6	0.45	99.9	31	66	2.6
KA2-2_05	60.7	24.7	0.26	0.004	6.4	7.5	0.46	100.1	31	66	2.7
KA2-2_06	58.5	26.2	0.25	0.009	8.1	6.7	0.34	100.1	39	59	2.0
KA2-2_07	60.7	24.8	0.19	0.001	6.5	7.7	0.43	100.3	31	66	2.5
KA2-2_08	62.4	23.8	0.14	0.004	5.2	8.2	0.59	100.3	25	72	3.4
KA2-1_01	58.6	26.1	0.25	0.012	8.1	6.7	0.31	100.1	39	59	1.8
KA2-1_02	57.7	26.8	0.34	0.007	8.9	6.2	0.26	100.3	43	55	1.5
KA2-1_03	58.9	25.9	0.28	0.011	7.8	6.8	0.31	100.1	38	60	1.8
KA2-1_04	60.8	24.7	0.25	0.014	6.4	7.6	0.41	100.1	31	67	2.4
KA2-1_05	59.4	25.7	0.25	0.014	7.5	7.1	0.35	100.2	36	62	2.0
KA2-1_06	60.4	25.0	0.21	0.008	6.6	7.5	0.45	100.1	32	65	2.6
KA2-1_07	63.1	22.9	0.13	0.000	4.4	8.5	0.68	99.6	21	75	3.9
KA2-3_01	53.3	30.0	0.21	0.003	12.4	4.4	0.12	100.4	60	39	0.7
KA2-3_02	53.8	29.4	0.21	0.007	11.7	4.6	0.16	100.0	58	41	0.9
KA2-3_03	53.4	29.4	0.25	0.005	11.9	4.7	0.13	99.8	58	41	0.8
KA2-3_04	60.7	24.6	0.17	0.009	6.2	7.7	0.40	99.8	30	67	2.3
KA2-3_05	59.8	25.3	0.23	0.006	7.0	7.1	0.36	99.9	34	63	2.1
KA2-3_06	60.0	25.2	0.23	0.003	7.0	7.1	0.42	100.0	34	63	2.4
KA2-3_07	61.5	24.3	0.21	0.003	5.9	7.8	0.48	100.1	29	69	2.8
KA2-3_08	62.7	23.6	0.15	0.003	5.0	8.3	0.59	100.2	24	73	3.4
KA2-3_09	62.0	24.1	0.17	0.004	5.5	8.1	0.57	100.5	26	70	3.3
KA2-3_10	63.1	23.6	0.17	0.000	4.8	8.4	0.62	100.7	23	73	3.6
KA2-4_01	59.9	25.1	0.24	0.009	6.8	7.4	0.42	99.8	33	65	2.4
KA2-4_02	58.9	25.9	0.30	0.005	7.8	6.8	0.36	100.0	38	60	2.1
KA2-4_03	58.1	26.2	0.31	0.008	8.3	6.6	0.30	99.7	40	58	1.7
KA2-4_04	59.7	25.2	0.24	0.003	7.0	7.2	0.38	99.7	34	63	2.2
KA2-4_05	62.0	23.7	0.18	0.006	5.2	8.1	0.58	99.8	25	72	3.3
KA2-4_06	62.2	23.9	0.19	0.000	5.4	8.0	0.54	100.1	26	70	3.2
KA2-4_07	63.3	22.8	0.13	0.000	4.3	8.5	0.71	99.7	21	75	4.1
KA3-1_01	59.0	26.0	0.21	0.006	7.7	6.9	0.36	100.0	37	61	2.1
KA3-1_02	59.1	25.7	0.28	0.005	7.7	6.9	0.33	100.1	38	61	1.9
KA3-1_03	52.8	29.9	0.32	0.008	12.5	4.3	0.13	100.0	61	38	0.8
KA3-1_04	55.1	28.7	0.36	0.010	10.8	5.3	0.19	100.4	53	46	1.1
KA3-1_05	59.5	25.6	0.31	0.009	7.4	7.0	0.33	100.1	36	62	1.9
KA3-1_06	60.2	25.0	0.22	0.000	6.9	7.4	0.39	100.1	33	64	2.3
KA3-1_07	61.5	23.9	0.16	0.006	5.5	8.1	0.53	99.7	27	70	3.0
KA3-1_08	63.0	22.7	0.15	0.003	4.3	8.6	0.74	99.5	21	75	4.3
KA3-2_01	62.0	24.0	0.19	0.008	5.5	8.1	0.53	100.3	26	71	3.0
KA3-2_02	62.1	23.8	0.18	0.005	5.4	8.1	0.54	100.1	26	71	3.1
KA3-2_03	62.0	24.0	0.21	0.008	5.5	8.1	0.53	100.3	26	71	3.0
KA3-2_04	62.4	23.6	0.20	0.011	5.1	8.3	0.56	100.2	25	72	3.2
KA3-2_05	60.4	24.8	0.23	0.010	6.4	7.6	0.41	99.9	31	66	2.4
KA3-2_06	59.9	25.2	0.26	0.000	6.9	7.3	0.40	100.0	33	64	2.3
KA3-2_07	62.2	23.5	0.18	0.004	5.0	8.3	0.59	99.7	24	72	3.4
KA3-2_08	63.2	22.9	0.18	0.006	4.4	8.4	0.73	99.9	21	74	4.2
KA3-6_01	60.2	25.0	0.24	0.009	6.8	7.4	0.38	100.0	33	65	2.2
KA3-6_02	60.4	25.0	0.21	0.004	6.6	7.4	0.39	100.0	32	66	2.2

KA3-6_03	60.9	24.7	0.18	0.000	6.4	7.6	0.43	100.1	31	67	2.5
KA3-6_04	61.7	24.3	0.21	0.003	5.8	8.0	0.51	100.4	28	69	2.9
KA3-6_05	63.0	23.3	0.17	0.004	4.7	8.6	0.65	100.4	22	74	3.7
KA3-6_06	63.8	22.8	0.13	0.000	4.3	8.7	0.75	100.6	20	75	4.3
Rotoma											
RM1-1_01	51.6	30.3	0.57	0.023	13.3	3.9	0.09	99.8	65	34	0.5
RM1-1_02	53.5	29.1	0.47	0.041	11.7	4.6	0.12	99.7	58	41	0.7
RM1-1_03	55.7	28.2	0.38	0.015	10.6	5.5	0.17	100.6	51	48	1.0
RM1-1_04	57.8	27.0	0.31	0.016	8.9	6.4	0.22	100.5	43	56	1.3
RM1-1_05	61.1	24.7	0.22	0.000	6.4	7.7	0.39	100.4	31	67	2.2
RM1-1_06	61.0	24.5	0.19	0.014	6.2	7.8	0.41	100.0	30	68	2.3
RM1-1_07	61.0	24.7	0.18	0.007	6.4	7.6	0.36	100.2	31	67	2.1
RM1-2_01	55.2	28.5	0.35	0.007	10.8	5.4	0.15	100.4	52	47	0.9
RM1-2_02	54.9	28.7	0.35	0.009	10.9	5.3	0.14	100.3	53	46	0.8
RM1-2_03	56.5	27.9	0.27	0.013	9.9	5.8	0.19	100.5	48	51	1.1
RM1-2_04	59.4	25.8	0.30	0.012	7.6	7.1	0.29	100.5	37	62	1.7
RM1-2_05	55.0	28.8	0.31	0.012	11.0	5.2	0.16	100.5	54	46	0.9
RM1-2_06	58.4	26.4	0.24	0.006	8.3	6.6	0.26	100.3	40	58	1.5
RM1-2_07	59.0	25.5	0.21	0.005	7.6	7.0	0.30	99.6	37	61	1.7
RM1-5_01	56.2	28.0	0.23	0.000	10.2	5.7	0.18	100.4	49	50	1.0
RM1-5_02	59.8	25.6	0.23	0.003	7.4	7.2	0.29	100.4	36	63	1.7
RM1-5_03	58.7	26.3	0.24	0.000	8.2	6.8	0.25	100.5	40	59	1.4
RM1-5_04	59.8	25.6	0.21	0.005	7.3	7.2	0.30	100.4	35	63	1.7
RM1-5_05	60.2	25.2	0.22	0.006	7.0	7.4	0.31	100.4	34	65	1.8
RM1-5_06	60.0	25.2	0.22	0.006	7.0	7.3	0.32	100.1	34	64	1.8
RM1-5_07	60.9	24.7	0.24	0.006	6.5	7.7	0.38	100.4	31	67	2.2
RM1-5_08	58.9	26.0	0.24	0.008	7.9	6.9	0.26	100.2	38	60	1.5
RM1-5_09	56.2	27.9	0.26	0.012	10.1	5.6	0.20	100.2	49	50	1.2
RM1-5_10	58.2	26.3	0.25	0.009	8.3	6.6	0.25	99.9	40	58	1.4
RM1-5_11	59.3	25.8	0.22	0.010	7.6	7.0	0.30	100.1	37	61	1.7
RM2-1_01	59.8	25.4	0.23	0.011	7.2	7.2	0.31	100.2	35	63	1.8
RM2-1_02	61.3	24.4	0.22	0.000	6.1	7.8	0.40	100.3	30	68	2.3
RM2-1_03	59.0	25.8	0.22	0.007	7.9	6.8	0.27	100.1	39	60	1.5
RM2-1_04	61.6	24.3	0.18	0.002	6.0	7.9	0.41	100.4	29	69	2.3
RM2-1_05	59.8	25.5	0.25	0.005	7.4	7.2	0.31	100.5	36	63	1.8
RM2-1_06	61.1	24.7	0.21	0.007	6.3	7.7	0.36	100.5	31	67	2.1
RM2-1_07	60.7	24.7	0.24	0.001	6.5	7.6	0.34	100.1	31	67	2.0
RM2-1_08	61.2	24.4	0.21	0.000	6.1	7.8	0.41	100.1	30	68	2.4
RM3-1_01	61.6	24.0	0.19	0.005	6.0	7.9	0.38	100.1	29	69	2.2
RM3-1_02	59.8	25.2	0.20	0.003	7.0	7.3	0.33	99.8	34	64	1.9
RM3-1_03	60.1	25.2	0.23	0.007	7.0	7.3	0.31	100.1	34	64	1.8
RM3-1_04	60.1	25.2	0.18	0.002	7.0	7.3	0.33	100.1	34	64	1.9
RM3-1_05	60.7	25.0	0.21	0.005	6.6	7.5	0.33	100.3	32	66	1.9
RM3-1_06	60.4	25.1	0.24	0.005	6.8	7.3	0.30	100.1	33	65	1.8
RM3-1_07	58.0	26.5	0.26	0.009	8.6	6.6	0.25	100.3	41	57	1.4
RM3-1_08	59.8	25.4	0.24	0.008	7.2	7.1	0.31	100.0	35	63	1.8
RM3-1_09	59.1	26.1	0.27	0.008	7.9	6.8	0.29	100.4	38	60	1.7